

## HYDRODYNAMICS OF COMETARY COMPACT H II REGIONS

S. J. A.<sup>1</sup>

Centro de Radioastronomía y Astrofísica, UNAM, Campus Morelia, Apartado Postal 3-72, 58090 Morelia, México

M. G. H

School of Physics and Astronomy, University of Leeds, LS2 9JT, UK

*Draft version November 9, 2018*

### ABSTRACT

We present numerical radiation-hydrodynamic simulations of cometary H II regions for a number of champagne flow and bowshock models. For the champagne flow models we study smooth density distributions with both steep and shallow gradients. We also consider cases where the ionizing star has a strong stellar wind, and cases in which the star additionally has a proper motion within the ambient density gradient. We find that our champagne flow plus stellar wind models have limb-brightened morphologies and kinematics which can see the line-of-sight velocities change sign twice between the head and tail of the cometary H II region, with respect to the rest frame velocity. Our bowshock models show that pressure gradients across and within the shell are very important for the dynamics, and that simple analytic models assuming thin shells in ram pressure balance are wholly inadequate for describing the shape and kinematics of these objects at early times in their evolution. The dynamics of the gas behind the shock in the neutral material ahead of the ionization front in both champagne flow and bowshock type cometary H II regions is also discussed. We present simulated emission-measure maps and long-slit spectra of our results. Our numerical models are not tailored to any particular object but comparison with observations from the literature shows that, in particular, the models combining density gradients and stellar winds are able to account for both the morphology and general radial velocity behavior of several observed cometary H II regions, such as the well-studied object G29.96–0.02.

*Subject headings:* H II regions — ISM: kinematics and dynamics — shock waves — stars:formation — stars:winds

### 1. INTRODUCTION

Massive stars are born in dense molecular clouds and modify their environment by the action of their ionizing photons and stellar winds. In a uniform medium a spherical H II region, or Strömgren sphere, will form (Strömgren 1939), which then expands due to the overpressure of the photoionized gas with respect to its surroundings (Kahn 1954). The earliest stages in the lives of high mass stars are generally invisible at optical wavelengths, since the star and its photoionized region remain embedded in the molecular cloud. These clouds are, however, optically thin to radio frequencies and infrared radiation and observations at these wavelengths have shown that uniform, spherical H II regions are the exception.

The survey at radio frequencies by Wood & Churchwell (1989) developed *IRAS* color criteria for embedded compact and ultracompact H II regions, which were used in later surveys (Kurtz et al. 1994). These surveys show that around 16% of the embedded H II regions have a cometary (i.e., head-tail) morphology, while an *IRAS*-selected methanol maser survey shows that 30% of ultracompact H II regions with methanol masers are cometaries (Walsh et al. 1998). Around 14% of much more evolved, optically visible H II regions, such as the Orion Nebula, also demonstrates cometary shapes at radio frequencies (Fich 1993). In fact, the Orion Nebula gives a clue as to the possible origin of the morphology of these objects since it is the archetype of the so-called “blister” H II regions identified by Israel (1978). Its close proximity and availability

for study at all wavelengths show us that the brightest part of the nebula corresponds to the ionization front on the surface of a molecular cloud, from which material is being photoevaporated. In the direction away from the cloud the nebula is open and ionized gas flows out into the diffuse intercloud medium.

The hydrodynamics of “blister” H II regions was modeled by Tenorio-Tagle and collaborators in a series of papers (Tenorio-Tagle 1979; Bodenheimer et al. 1979; Bedijn & Tenorio-Tagle 1981; Yorke et al. 1983), who renamed them “champagne” flows. Later, the effects of including a stellar wind in this scenario were studied by Comerón (1997). In both of these studies an H II region evolving in a uniform, dense cloud breaks out into the diffuse intercloud medium once the ionization front reaches the edge of the cloud. Ionized gas accelerates out of the H II region reaching velocities up to  $\sim 30 \text{ km s}^{-1}$ .

For H II regions still embedded in their natal clouds, the classification “compact” is applied to those whose size scales are in the range 0.1–0.3 pc and “ultracompact” to those whose sizes are  $< 0.1 \text{ pc}$ . It is thought that these regions, because of their small size, represent early stages in the lifetime of the star ( $< 10^5 \text{ yrs}$ ) before the H II region has expanded out of the cloud. If a compact H II region is still wholly contained within a molecular cloud, a “blister” scenario cannot strictly be applied since the ionized region has not reached the edge of the cloud. Instead, it could be envisaged that the champagne flow occurs due to a density gradient within the cloud. (The density gradient could be a relic of the cloud-collapse process that produced the massive star.) Garcia-Segura & Franco (1996) studied the morphologies that arise when ionization fronts form in stratified media and spherical density distri-

Electronic address: j.arthur@astrosmo.unam.mx  
Electronic address: mgh@ast.leeds.ac.uk

<sup>1</sup> Work partially carried out while on sabbatical leave at the School of Physics and Astronomy, University of Leeds, UK

butions, and the instabilities to which they are subject when cooling and stellar winds are included. The hydrodynamics of photoevaporated champagne flows in density gradients was investigated by Henney et al. (2005), who found that long-lived quasi-stationary flows are set up in which the ionized flow is steady in the frame of the ionization front.

Observational studies of molecular clouds show that they are centrally condensed, with moderate-density envelopes ( $10^3$ – $10^5$  cm $^{-3}$ ) surrounding high-density cores ( $10^7$  cm $^{-3}$ ), suggesting strong density gradients within the clouds (Hofner et al. 2000). Molecular line studies of dark clouds show that the density gradients can be approximated by power-laws  $\rho(r) \propto r^{-\alpha}$ , with exponents ranging from 1 to about 3 (Arquilla & Goldsmith 1985). Near-infrared dust extinction studies of dark clouds show similar results (e.g., Teixeira et al. 2005). Studies of the extended sub-millimeter dust emission around ultracompact H II regions also display power-law density structures, with the exponent varying between 1.25 and 2.25 (Hatchell & van der Tak 2003). In these studies,  $\alpha$  equal to 2 is the most commonly found value for the power-law exponent, which corresponds to an isothermal, self-gravitating sphere. Analysis of the radio continuum spectra of three highly compact H II regions by Franco et al. (2000) also imply negative power-law density distributions with exponent  $\alpha \geq 2$ , possibly even as steep as  $\alpha = 4$  in one case. These hyper and ultracompact H II regions are considered to represent the earliest stages of H II region evolution, and so provide information about the natal cloud density distribution. Once the H II region has begun to expand, the density distribution of the ionized gas will become shallower as structure within the H II region is smoothed out on the order of a sound crossing time. Thus, the density gradients reported by Franco et al. (2000) should be treated as lower limits to the initial density gradients in the star-forming cores. For the largest values of  $\alpha$  reported, such a steep radial, power-law density distribution is unlikely and it is possible that the density stratification is better represented by a Gaussian or other exponential function. Power-law density gradients with exponents  $1.6 < \alpha < 2.4$  are also reported for giant extragalactic H II regions (Franco et al. 2000), showing that density gradients should be taken into consideration at all stages of H II region evolution.

An alternative explanation for the cometary shape of some compact H II regions is that the ionizing star is moving with respect to the dense cloud gas. Mac Low et al. (1991) and van Buren & Mac Low (1992) developed a bowshock interpretation for cometary compact H II regions, in which the ionizing star with its strong stellar wind is moving supersonically with respect to the cloud gas and the ionization front becomes trapped in the swept-up shell behind the bow shock that forms ahead of the star. Numerical models of supersonically moving high mass stars have been carried out by Raga et al. (1997) and Comerón & Kaper (1998) in the context of runaway O stars in the diffuse interstellar medium. Even though the parameters are not appropriate for young massive stars moving in dense molecular clouds, these numerical models show that instabilities complicate the dynamics. Recent numerical models of H II regions around massive stars orbiting in the gravitational potential of structured molecular clouds (but without including the stellar winds) have been done by Franco et al. (2005), who show that a wide variety of unpredictable morphologies can result.

Bowshock models are attractive because they easily reproduce the limb-brightened morphology seen in radio continuum images of cometary compact H II regions, whereas

champagne flows have no limb brightening. However, it is in the kinematics of the ionized gas that these two scenarios can really be distinguished. In the bowshock model the highest ionized gas velocities are at the head and are equal to the star’s velocity. In the champagne flow model the highest ionized gas velocities are found in the tail and can reach a few times the sound speed. Unfortunately, observational kinematical studies are difficult to perform given the complete extinction that exists in the optical due to the dense environments in which these objects are found. Radio recombination line studies (Wood & Churchwell 1991; Afflerbach et al. 1994; Garay et al. 1994; Cyganowski et al. 2003), infrared recombination line observations (Lumsden & Hoare 1996, 1999; Hoare et al. 2003; Martín-Hernández et al. 2003), and mid-infrared fine-structure line observations (Jaffe et al. 2003; Zhu et al. 2005) have, however, been able to extract some kinematical information from these regions, which should enable us to distinguish between the various theoretical models that have been put forward to explain this phenomenon. It is important to obtain a good determination of the background molecular cloud velocity, which can have a major effect on the interpretation of the observations.

The kinematical observations available suggest that neither a bowshock model nor a champagne flow adequately explain the velocity variation between head and tail of many observed cometary H II regions, or between the center and the wings. Gaume et al. (1994) highlighted the need for more realistic models, incorporating stellar winds and more complicated ambient density distributions in the surrounding molecular cloud. Lumsden & Hoare (1999) proposed an empirical model for the well-studied object G29.96–0.02 in which a champagne flow is modified by the presence of a strong stellar wind within the H II region which traps the H II region in the denser gas into a swept-up shell and diverts the photoevaporated flow around the hot stellar wind bubble. They also required a component of expansion into the molecular cloud of  $\sim 10$  km s $^{-1}$ . Zhu et al. (2005) discuss the need for pressure gradients within a paraboloidal shell to explain the velocity range for this object.

In addition to the H II region dynamics, hot, massive stars possess strong stellar winds, which will also affect the velocity structure of these regions. Work by Garcia-Segura & Franco (1996) and Freyer et al. (2003) has shown that the interaction of the photoionized region with a swept-up stellar wind shell produces all sorts of interesting structures, such as spokes, shells, clouds and fingers. These arise due to cooling, thin shell, Rayleigh-Taylor and other instabilities, which have been analyzed by Vishniac (1983), Ryu & Vishniac (1988) and Vishniac (1994). The shapes of stellar wind bubbles forming in H II regions with density gradients was studied analytically by Dyson (1977). That cometary, compact H II regions also contain stellar winds is evident from observations of our nearest compact H II region, the Orion Nebula. The size scale of the Orion nebula is a few tenths of a parsec in diameter. *Hubble Space Telescope* (HST) observations of the nebula reveal the presence of bowshocks ahead of the photoevaporating circumstellar material around the “proplyds” (protoplanetary disks) in the direction directly towards the main ionizing star of the nebula,  $\theta^1$  C Ori. These bowshocks are direct evidence of an interaction between the photoevaporated flows within the nebula and the strong stellar wind from the ionizing star and enable us to constrain  $\dot{M}V_w$  of the stellar wind (García-Arredondo et al. 2001, 2002).

In this paper we investigate the formation and evolution of

cometary compact H II regions both with and without stellar winds in a variety of ambient density distributions and compare these results to kinematic data from the literature. The organization of the paper is as follows: in § 2 we describe our numerical model and test cases, while in § 3 we describe a set of basic reference models comprising a simple champagne flow, a bowshock in a uniform medium, and a champagne flow with a stellar wind. In § 4 we describe modifications to these basic models, including varying the steepness of the density gradient and the strength of the stellar wind, and adding stellar motion to the champagne flow plus stellar wind models. We discuss our results in the context of other models and briefly compare our results to observations taken from the literature in § 5. Finally, in § 6 we conclude our findings.

## 2. NUMERICAL MODEL

### 2.1. Method

We need to calculate both the hydrodynamics and the radiative transfer within the cometary H II regions. This is a non-trivial problem involving a variety of timescales.

For the radiative transfer we adopt a similar procedure to that used in Raga et al. (1999), which uses the method of short characteristics (Mihalas et al. 1978; Kunasz & Auer 1988) to calculate the column density from every source point to each point on the numerical grid, and thence the photoionization rate at each point. We have adapted this method, described in Raga et al. (1999) for a three-dimensional Cartesian system, to a two-dimensional cylindrically symmetric system. In the models presented in this paper we consider only a single source point (i.e., the star) for the ionizing radiation. The ionizing flux is calculated from the number of photons with energies above the hydrogen ionization threshold of 13.6 eV produced by a simple black body of a given effective temperature and stellar radius. Only one frequency of radiation is included in the radiative transfer and the diffuse field is treated by the on-the-spot approximation (Henney et al. 2005).

The hydrodynamics is treated with a two-dimensional, cylindrically symmetric hybrid Godunov-van Leer second order method (Godunov 1959; Arthur & Falle 1993; van Leer 1982). A hybrid method is used in order to avoid the ‘‘carbuncle’’ instability seen behind shocks parallel to grid lines with purely Riemann solver codes (see, e.g., Quirk 1994). Van Leer and Riemann solver steps are alternated. The Van Leer scheme is not strictly upwind according to the definition of Sanders et al. (1998) and puts a small shear term into the momentum equation. This shear dissipation is sufficient to overcome the carbuncle instability. On the other hand, a Riemann solver does a more accurate job in general of representing the flow, particularly in transonic regions, and so the combined scheme has the benefits of both methods without their respective disadvantages.

The hydrodynamics and radiative transfer are coupled through the energy equation, where the source term depends on the photoionization heating and the radiative cooling rates. The radiative cooling includes collisional excitation of Lyman alpha, collisional excitation of neutral and ionized metal lines (assuming standard ISM abundances), hydrogen recombination, collisional ionization and bremsstrahlung, with each cooling process being characterized by an analytic approximation which depends on temperature and ionization fraction. The energy equation is solved explicitly using a second order Runge-Kutta method. In photoionization equilibrium the gas temperature in our models is  $10^4$  K. The time step for the calculations is the minimum of the hydrodynamic (Courant

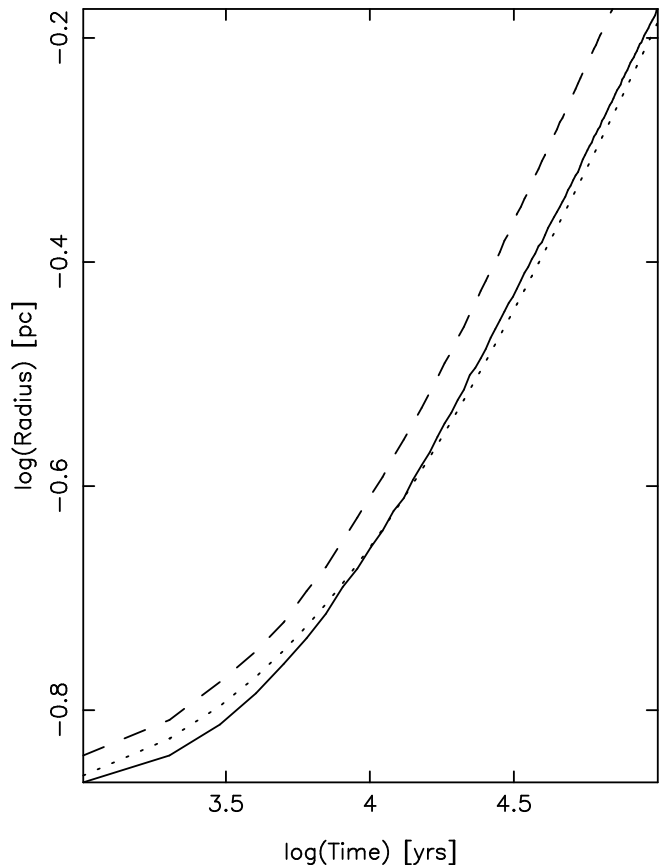


FIG. 1.—Expansion as a function of time of the ionization front (solid line) and preceding shock front (dashed line) for an H II region in a uniform density medium. The dotted line represents the analytical expansion law (Spitzer 1978) for the same parameters.

condition) and cooling times, evaluated at each time step. The present models do not include thermal conduction nor absorption of ionizing photons by dust grains. The presence of dust within an H II region can have a dramatic effect on the size of the Strömgen sphere. However, the distribution of dust within the H II region depends strongly on the gas density and stellar spectrum and there can even be quite a large volume devoid of grains due to sublimation (Arthur et al. 2004). Such complications are beyond the scope of this paper.

### 2.2. Test cases

#### 2.2.1. Expansion of an H II region in a uniform density medium

We modeled the expansion of the H II region produced by a 30,000 K black body in a uniform medium of density  $6000 \text{ cm}^{-3}$  and initial temperature 300 K. The ionizing photon rate of the source is  $Q_{\text{H0}} = 2.2 \times 10^{48} \text{ s}^{-1}$  and the theoretical initial Strömgen sphere has a radius of  $R_s = 0.124 \text{ pc}$  for an ionized gas temperature of  $T = 10,000 \text{ K}$ . Our numerical model also has a Strömgen radius of  $R_{\text{ns}} = 0.124 \text{ pc}$ , for an ionized gas temperature of  $T \approx 10,500 \text{ K}$ . Once formed, this overpressured sphere of gas begins to expand into the surrounding medium. An analytical approximation to the expansion (Spitzer 1978) is

$$R_i = R_s \left( 1 + \frac{7}{4} \frac{c_{\text{II}} t}{R_s} \right)^{4/7} \quad (1)$$

where  $c_{\text{II}}$  is the sound speed in the ionized gas,  $R_i$  is the ionization front radius and  $t$  is time, under a set of simplifying assumptions, including (i) that the swept-up neutral shell between the shock wave and ionization front is thin such that the shock and ionization front move with the same velocity (ii) the pressure across the neutral shell is uniform. At late times the expansion law is characterized by  $R_i \propto t^{4/7}$ .

In Figure 1 we show the numerical results of a 2D cylindrically symmetric simulation with grid resolution  $512 \times 1024$  cells for the shock front and ionization front radii as a function of time, together with the analytic result for the same initial parameters. At early times the analytic and numerical solutions differ because the rarefaction wave that propagates back through the H II region when the expansion first starts in the numerical model reduces the pressure in the ionized gas and hence the numerical solution lags behind the analytical one to start with. After 10,000 yrs the numerical and analytic results agree but then begin to deviate slightly, with the numerical solution being ahead of the analytical one at these times. This is because the assumptions made for the analytic expansion break down. The neutral shell ceases to be thin because the shock propagates faster than the ionization front. In particular, the density just ahead of the ionization front decreases as a fraction of the average density in the neutral shell as time goes on, meaning that the ionization front is propagating into a successively less dense medium with time, and hence the expansion is faster than that predicted by the analytic formula, which does not allow for any evolution of conditions in the neutral shell.

### 2.2.2. Expansion of an H II region in the presence of a stellar wind

The expansion of a stellar wind into a surrounding environment has been studied numerically by many authors (e.g., Falle 1975; Garcia-Segura & Mac Low 1995; Garcia-Segura et al. 1996). In one-dimensional studies the textbook regions of unshocked wind, shocked wind, swept-up shocked ISM are easily distinguished (Dyson & Williams 1997; Weaver et al. 1977). However, once studies are extended to two dimensions, thin shell instabilities in the cooling swept-up ISM lead to a more complex appearance, which could influence the H II region outside (Garcia-Segura & Mac Low 1995; Garcia-Segura et al. 1996; Garcia-Segura & Franco 1996; Comerón 1997; Freyer et al. 2003). In particular, the knotty appearance of the unstable thin shell leads to shadowing by clumps of the H II region. The resulting pressure variations between shadowed and unshadowed regions lead to complicated, low velocity ( $\leq 20 \text{ km s}^{-1}$ ) kinematics in the ionized gas.

We used a Chevalier & Clegg (1985) stellar wind model to input the initial stellar wind conditions as a volume-distributed source of mass and energy (this method for dealing with the stellar wind was also used by Rozyczka 1985; Comerón 1997). This avoids the problem of reverse shocks that occur when the stellar wind is input simply as a region of high density, high velocity flow near the origin. The mass and energy source terms were calculated so as to give the correct mass-loss rate and terminal velocity for the stellar wind. The volume occupied by stellar wind source terms was chosen to be sufficiently small so that the stellar wind always reached its terminal velocity and shocked outside of the source region, but sufficiently large so as to be a reasonable geometrical representation of a sphere on a cylindrical grid. Of course, this thermal wind is not the same as a pressureless stellar wind at the center of the inner unshocked wind region, but it does

have the same ram pressure. The Mach number of the thermal wind just before the inner stellar wind shock is  $\sim 10$ , and so is highly supersonic, meaning that any thermal pressure in this region is not dynamically important.

We performed a number of studies of the evolution of H II regions around stellar wind bubbles with the aim of establishing the optimum resolution for our calculations. The high densities ( $\approx 6000 \text{ cm}^{-3}$ ) in the ambient gas imply extremely short cooling times, requiring a short time step for adequate resolution. In addition, a fast stellar wind also requires a short time step due to the high temperatures (and hence sound speeds) in the shocked wind region.

On our two-dimensional grids we could not hope to achieve the resolution necessary to fully resolve the cooling shocked swept-up ISM shell. However, by reducing the cooling rate and heating due to photoionization by a given factor we can maintain the temperature in the ionized gas while artificially enhancing the resolution in the cooling shell (by increasing the cooling length). This means that radiative cooling in the shell occurs more slowly than it would otherwise have done so, but given the densities involved, cooling is still rapid in these simulations. We then examined a number of simulations at different grid resolutions in order to determine a consistent qualitative behaviour in the cooling region. Note that in these simulations there is no need to trigger instabilities in the swept-up shell with density fluctuations (e.g., Garcia-Segura et al. 1996) because the cylindrical symmetry means that the stellar wind source volume introduces its own numerical noise simply by not being perfectly spherical. Furthermore, we artificially broaden the ionization front (by reducing the ionization cross-section), in order to avoid artificial numerical instabilities generated at the grid scale (Williams 1999).

In Figure 2 we show the evolution of the ionized density in the region surrounding a (blackbody) star of effective temperature  $T_{\text{eff}} = 30,000 \text{ K}$ , stellar wind mass-loss rate  $\dot{M} = 10^{-6} M_{\odot} \text{ yr}^{-1}$  and terminal velocity  $V_w = 2000 \text{ km s}^{-1}$ , where the initial ambient medium has number density  $n_0 = 6000 \text{ cm}^{-3}$  and temperature  $T_0 = 300 \text{ K}$ . The ionizing photons and the stellar wind are started simultaneously. The top four panels show the ionized density at times 200, 500, 1000 and 1500 years since the start of the calculation with grid resolution  $400 \times 400$  cells. The grid shown represents a spatial size of  $0.15 \times 0.15$  parsecs. The H II region forms essentially immediately, on a recombination timescale, with a radius of 0.13 parsecs. The stellar wind bubble takes longer to form and will grow until balance is achieved between the ram pressure of the stellar wind and the thermal pressure of the surrounding ISM.

By the time of the first panel (200 years), instabilities have begun to form in the swept up shell of ionized gas, at 0.03 parsecs radius. The rapid cooling in this shell means that it is thin and subject to the thin shell and Vishniac instabilities (Vishniac 1983; Ryu & Vishniac 1987, 1988; Vishniac & Ryu 1989; Vishniac 1994), which have been shown to occur in 2D numerical stellar wind bubble models (Garcia-Segura & Mac Low 1995; Garcia-Segura & Franco 1996; Freyer et al. 2003). The ionized densities in the shell reach  $10^5 \text{ cm}^{-3}$ , i.e., compression factors much higher than the factor 4 expected for an adiabatic shock, confirming that this is a region of strong cooling. The increased opacity due to the swept-up shell leads to recombination of the ionized region beyond. The inhomogeneities in the shell represent opacity variations, which lead to variations in the recombination rate that can be detected as

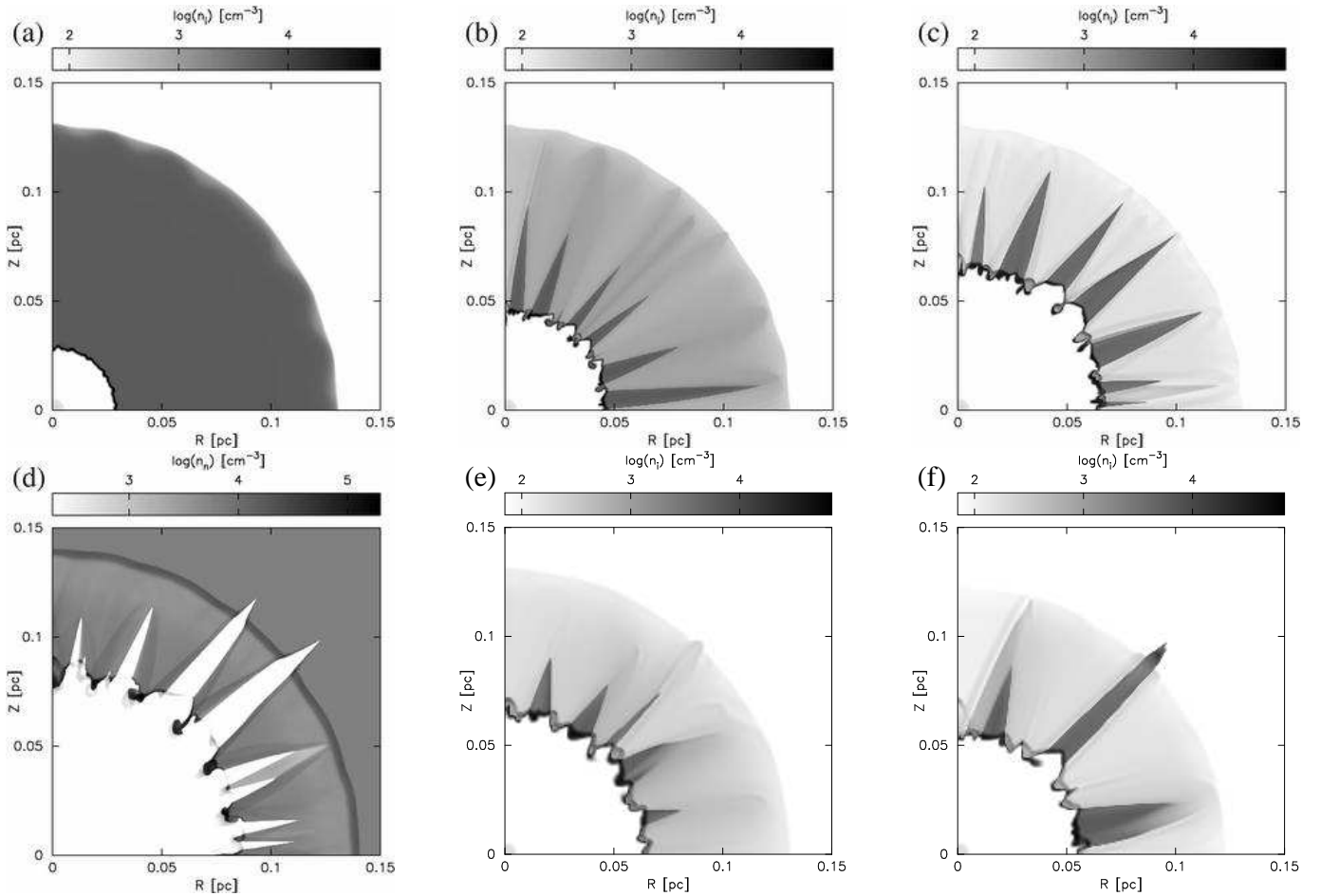


FIG. 2.— Evolution of  $\log_{10}(\text{density})$  in an H II region with a stellar wind. Grayscale for the ionized gas covers the range  $70 < n_i < 70000 \text{ cm}^{-3}$ , while for the neutral gas the grayscale range is  $200 < n_n < 200000 \text{ cm}^{-3}$ . (a) Ionized gas density after 200 years (full range  $0 < n_i < 11700 \text{ cm}^{-3}$ ), showing the formation of ripples in the swept-up thin shell due to cooling instabilities and corrugations in the ionization front due to shadowing. (b) Ionized gas density after 500 years ( $0 < n_i < 92400 \text{ cm}^{-3}$ ) showing the growth of the shadowing instability. (c) Ionized gas density after 1000 years ( $0 < n_i < 61100 \text{ cm}^{-3}$ ). (d) Neutral gas density after 1500 years ( $0 < n_n < 210000 \text{ cm}^{-3}$ ) showing the formation of dense neutral clumps at the base of the ionized spokes. (e) Same as (c) but at half the grid resolution ( $0 < n_i < 45200 \text{ cm}^{-3}$ ). (f) Same as (e) but with a larger cooling coefficient ( $0 < n_i < 63000 \text{ cm}^{-3}$ ).

ripples in the outer rim.

In the second panel (500 years), the instability has saturated and the knotty thin shell at 0.045 parsecs is being pushed outwards by the hot, shocked stellar wind bubble. The degree of ionization in the H II region beyond the swept-up shell is very small as this region has now essentially completely recombined. The knotty nature of the thin shell causes variations in the optical depth and this leads to the shadowing instability discussed by Williams (1999). Spokes of ionized gas are characteristic of this instability and represent the propagation of R-type ionization fronts in collimated beams through gaps (regions of underdensity) in the knotty shell. The bases of the beams are wider than the tips because the ionized gas at the base is pressurized and the gas can expand laterally. The freely flowing and shocked stellar wind regions interior to the swept-up shell are of such low density that they do not contribute to the map of ionized density despite being fully ionized regions.

In the third (1000 years) and fourth (1500 years) panels the knotty shell has expanded outwards pushed by the hot shocked stellar wind, reaching a mean radius of 0.08 parsecs in panel four. The dense clumps of neutral gas that form at the base of the ionized spokes are the result of the shadowing in-

stability (Williams 1999). Their density continues to increase as time goes on, unlike the ionized gas density in the swept-up thin shell, which decreases since the pressure in this region decreases as the expansion proceeds (the temperature of this gas remains constant at  $10^4 \text{ K}$ ). The main ionization front is trapped in the swept-up stellar wind shell at these times. As the expansion of the stellar wind bubble proceeds, the movement of the knots, plus the contributions to the opacity of the material photoevaporating from the neutral clumps, lead to changes in the pattern of spokes.

The shadowing instability discussed by Williams (1999) results from the effect on an R-type ionization front of inhomogeneities in the upstream density. First, corrugations in the ionization front are formed, which become amplified by the instability, leading to the formation of characteristic spokes of ionized gas with clumps of dense, neutral material at the base. In the simulations presented in Figure 2, the shadowing effect is produced by clumps formed by the thin-shell instability in the swept-up stellar wind shell, within the H II region itself. Although corrugation of the outer ionization front is seen at early times (Fig. 2a), this is not important for the growth of the instability, since the whole region outside of the thin shell is recombining by this point. The shadowing instability takes

TABLE 1  
 M

Model	$n$	$n_0$ cm <sup>-3</sup>	$H$ pc	$\dot{M}$ $M_\odot$ yr <sup>-1</sup>	$V_w$ km s <sup>-1</sup>	$V_*$ km s <sup>-1</sup>
A	$n_0 \exp(z/H)$	8000	0.05	...	...	...
B	$n_0$	6000	...	$10^{-6}$	2000	20
C	$n_0 \exp(z/H)$	8000	0.05	$10^{-6}$	2000	...
D	$n_0 \exp(z/H)$	8000	0.05	$10^{-7}$	2000	...
E	$n_0 \exp(z/H)$	8000	0.2	$10^{-6}$	2000	...
F	$n_0 [1 + (R/0.01)^2]^{-1}$	$9.8 \times 10^6$	...	$10^{-6}$	2000	...
G	$n_0 \exp(z/H)$	8000	0.05	$10^{-6}$	2000	5
H	$n_0 \exp(z/H)$	8000	0.05	$10^{-6}$	2000	10
I	$n_0 \exp(z/H)$	8000	0.2	$10^{-6}$	2000	10

hold within the thin shell itself, where the main ionization front has become trapped. Because the whole structure is expanding due to the high pressure of the shocked stellar wind, the pattern of ionized spokes in our simulations changes with time.

The fifth panel of Figure 2 shows the effects of reducing the grid resolution. Reducing the resolution by a factor 2 in each dimension gives qualitatively similar results to the standard case.

In the sixth panel we have used the full value of the cooling rate and heating rate with the lower grid resolution. Increasing the cooling and heating rates means that cooling occurs sooner and more quickly, leading to a thinner, denser swept-up shell. The recombining region has receded to 0.12 parsecs by 1000 years of evolution while the swept-up wind shell is located at 0.05 parsecs from the central star, as compared to 0.06 parsecs in the standard case. However, for this grid resolution the shell is certainly not resolved and would require much higher resolution. In these calculations it is desirable to resolve the shell as well as possible because of the effect this has on the ionized region beyond. The device of decreasing the cooling and heating rates permits us to better resolve the swept-up shell without having to use an unpractical number of grid cells.

### 3. BASIC MODELS

Our models are motivated by a desire to explain features of the spectra of cometary ultracompact H II regions such as G29.96–0.02, whose morphology and kinematics cannot satisfactorily be explained by either a simple champagne flow or a simple bowshock model. In particular, we are interested in explaining the turnover from blueshifted to redshifted to blueshifted velocity seen going from the head to the tail along the symmetry axis in observations of this object in hydrogen recombination lines (see, e.g., Lumsden & Hoare 1996, 1999; Martín-Hernández et al. 2003) and fine-structure lines of the Ne<sup>+</sup> ion (Zhu et al. 2005).

Instead of tailoring a model to fit a particular observation, in this paper we wish to identify features in the simulated spectra that correspond to different configurations of density distribution, stellar wind parameters and stellar motion. To this end, we consider only one set of parameters for the ionizing star, namely a 30,000 K black body with an ionizing photon rate of  $2.2 \times 10^{48}$  s<sup>-1</sup>. This corresponds approximately to spectral type O9V (Panagia 1973; Martins et al. 2005). The ambient medium is taken to be at rest and neutral, with a temperature of 300 K. For the majority of models, the grid resolution is

750 × 1000 cells, representing a total grid size of 0.6 × 0.8 parsecs.

To begin with we discuss three “canonical models”, Models A, B, and C of Table 1, which correspond to a simple champagne flow, a stellar bowshock in a uniform medium, and a champagne flow with a stellar wind, respectively. The model parameters are summarized in Table 1. Model A is followed for 20,000 yrs, while Models B and C are evolved for 40,000 yrs.

#### 3.1. Model Parameters

##### 3.1.1. Champagne flow: Model A

We set up a photoevaporated flow in an exponential density distribution, where the density at the position of the source is  $n_0 = 8000$  cm<sup>-3</sup> and the scale height is  $H = 0.05$  pc.

##### 3.1.2. Bow Shock: Model B

The source is assumed to move with a velocity of 20 km s<sup>-1</sup> in a uniform medium of density  $n_0 = 6000$  cm<sup>-3</sup>. This velocity is motivated by previous empirical models (e.g., Afflerbach et al. 1994; Lumsden & Hoare 1996; Martín-Hernández et al. 2003; Zhu et al. 2005) for the ultracompact H II region G29.96–0.02. This star has a strong stellar wind with mass loss rate  $\dot{M} = 10^{-6} M_\odot$  yr<sup>-1</sup> and terminal velocity  $V_w = 2000$  km s<sup>-1</sup>, typical of an early type star. After the 20,000 yrs of evolution followed by the simulation, the star has traveled a distance of 0.4 pc. The resolution of this model is 512 × 1024 cells, representing a spatial size of 0.4 × 0.8 parsecs.

##### 3.1.3. Champagne flow with stellar wind: Model C

We investigate the effect of including a stellar wind in the champagne flow described in Model A. The stellar wind has a mass loss rate  $\dot{M} = 10^{-6} M_\odot$  yr<sup>-1</sup> and terminal velocity  $V_w = 2000$  km s<sup>-1</sup>, i.e., the same wind parameters as used in the standard bowshock model.

#### 3.2. Basic model results

##### 3.2.1. Velocity field

Figures 3, 4 and 5 show the logarithm of the ionized density (greyscale) and velocity field in the  $r - z$  plane for each of the canonical models A (champagne flow), B (bowshock), and C (champagne flow plus stellar wind) described in Table 1 after 10,000 yrs, 20,000 yrs and (for Models B and C) 40,000 yrs of evolution. The velocity field is represented by a split scale: the black arrows show the highest velocity gas  $v > 30$  km s<sup>-1</sup>

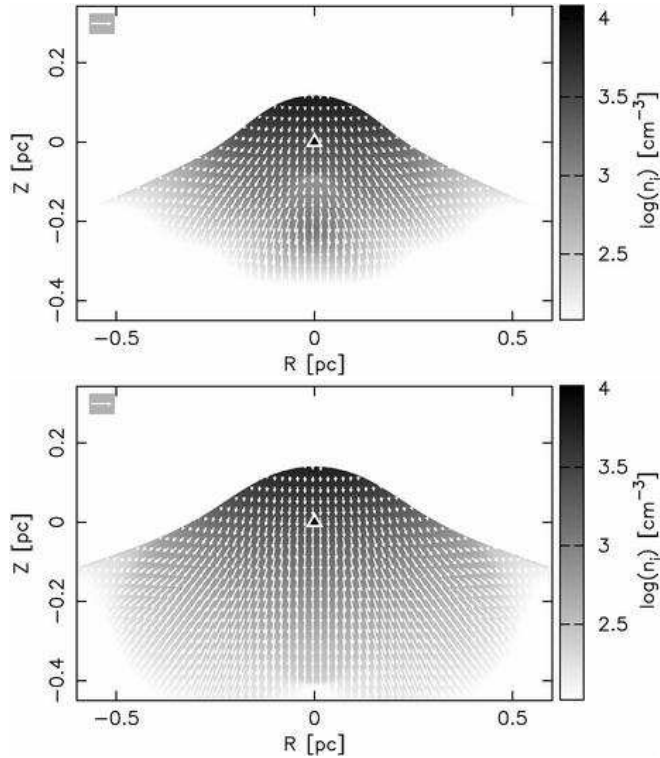


FIG. 3.— Logarithm of ionized density for a cut through the  $r-z$  plane of the numerical simulation of Model A (simple champagne flow) after elapsed times of 10,000 yrs (top panel) and 20,000 yrs (bottom panel). The arrows show the velocity field, with the scale arrow representing  $30 \text{ km s}^{-1}$  in these models. The position of the source is marked by a black triangle.

(generally representing stellar wind gas), while the white arrows are scaled to the lower velocity gas  $v \leq 30 \text{ km s}^{-1}$  (present in the photoevaporated flows and swept up shells). The grayscale shows the densest ionized gas in black with a dynamic range of 2 orders of magnitude. Neutral gas, or very low density ionized gas (i.e., stellar wind) appears white.

From these figures we see that in the case of the pure champagne flow, Model A, the ionization front is smooth, whereas that of Model C, which has a stellar wind, has a rippled appearance due to the formation of instabilities in the swept-up wind shell, such as those presented in Figure 2 and discussed above. In Model B, the ionization front becomes trapped in the swept-up wind shell, which forms a bowshock ahead of the moving star. In Model C the ionization front is trapped ahead of the star in the denser gas but escapes at the sides where the density is lower and forms a champagne flow here. As regards temporal evolution, we see from Figure 3 that the champagne flow model (Model A) does not appreciably change in appearance between the two times depicted. This quasi-stationary phase was described by Henney et al. (2005) and the ionization front advances very slowly ( $\sim 2 \text{ km s}^{-1}$ ) up the density gradient. At the earlier time, the champagne flow has not completely cleared the low-density material from the grid: the rarefaction wave moving back from the initial Strömgen surface through the ionized gas when the H II region begins to expand hydrodynamically reaches the symmetry axis earlier where the ionization front shape is narrower. This shows up as a “bump” in the velocity distribution of the upper panel of Figure 3. By the time 20,000 yrs have passed, the rarefaction wave has reached the symmetry axis at all  $z$

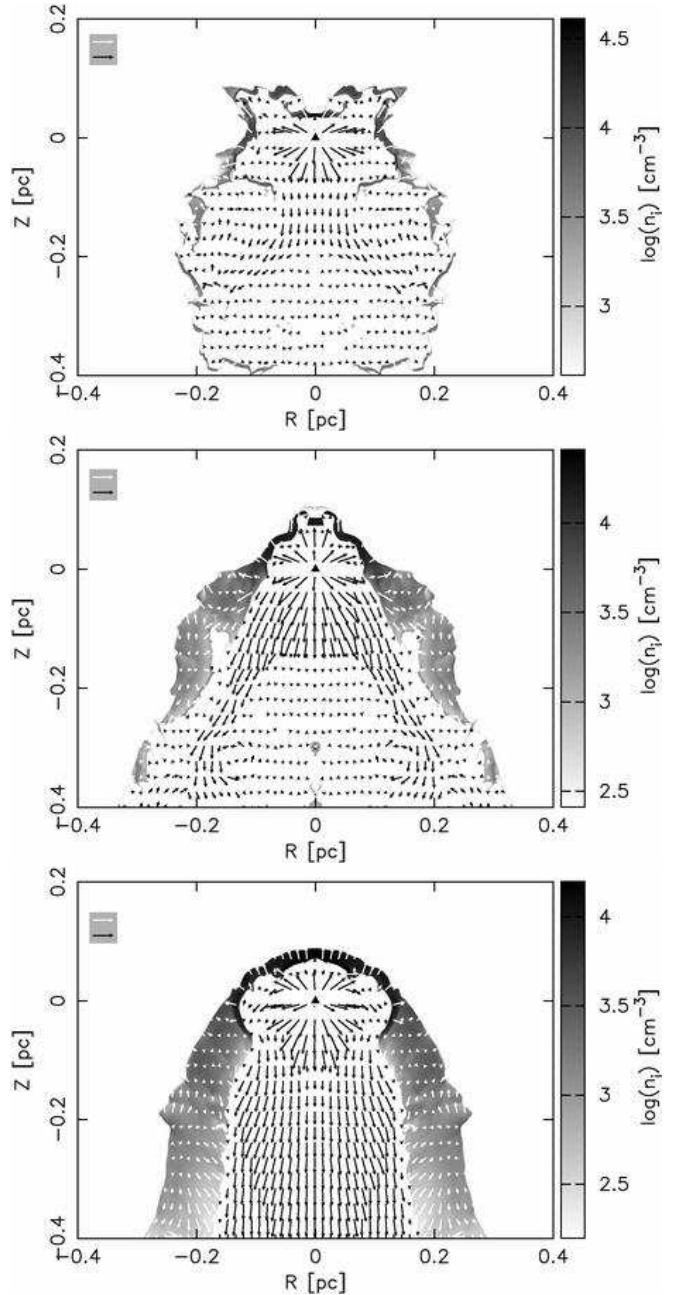


FIG. 4.— Same as Figure 3 but for Model B (simple  $20 \text{ km s}^{-1}$  bowshock model) and showing evolution after 10,000 yrs (top panel), 20,000 yrs (middle panel) and 40,000 yrs (bottom panel). The black arrows represent velocities of  $30 < v \leq 2000 \text{ km s}^{-1}$  in this figure, while the white arrows represent velocities of  $v \leq 30 \text{ km s}^{-1}$ .

heights and the champagne flow fills the whole grid. We note that for this model we do not see the shadowing instability discussed in § 2.2.2 because the initial conditions are totally smooth and there is no stellar wind shell to form clumps.

In Figure 6 we can see how the presence of a strong stellar wind affects a champagne flow. The initial ionization front distance ahead of the star for Models A and C is the same, reflecting the fact that the ionized region is set up within one recombination time of the star switching on. The ionization front distance in Model C then retreats, which corresponds to the formation of the dense swept-up stellar wind shell that traps the ionization front. At these very early times

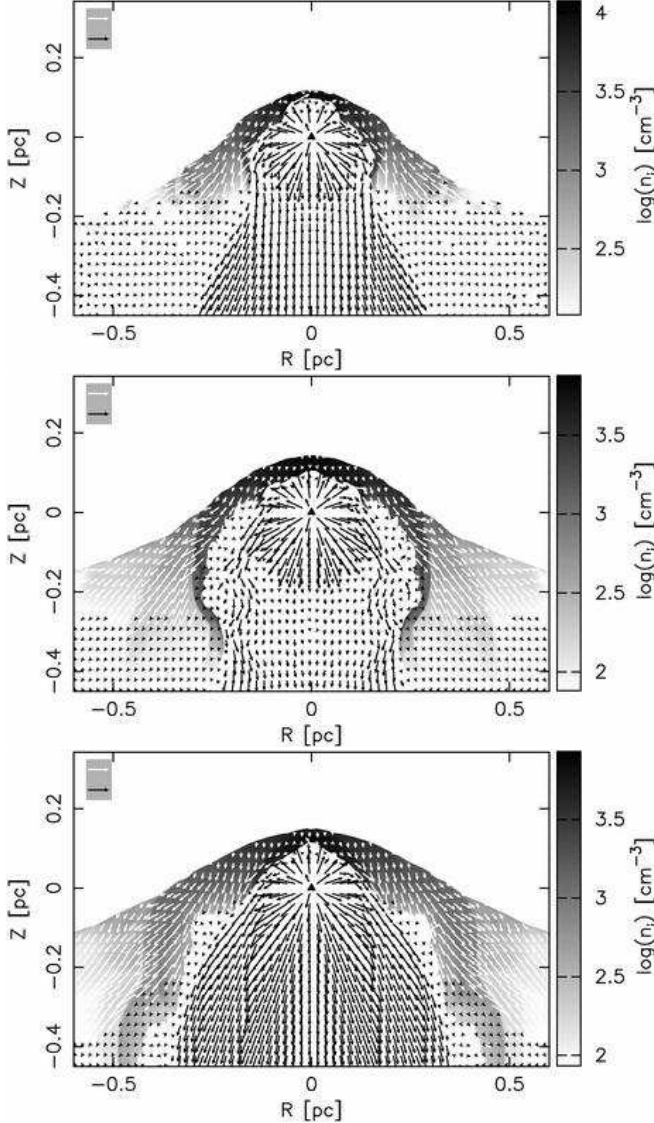


FIG. 5.— Same as Figure 4 but for Model C (champagne flow plus strong stellar wind).

( $t < 4000$  yrs), before the density gradient has become important, the shadowing instability produces spokes of ionized gas protruding beyond the swept-up shell. However, once the bubble diameter is greater than about one density scale height, the strong advection around the shell due to the density gradient means that any clumps that could cause shadowing are moving too fast for the instability to take effect. The initial shadowing does open up “holes” in the thin shell, through which the hot, shocked stellar wind can flow, generating a turbulent interface. As the hot, pressurized, energy-driven stellar wind bubble expands supersonically, the ionization front advances up the density gradient and after 5000 yrs has caught up with the simple champagne flow ionization front. Eventually, in the direction of decreasing density the stellar wind bubble blows out, and there is a transition to a momentum-driven flow. Meanwhile, a champagne flow starts to establish itself within the swept-up shell. Initially, the champagne flow is blocked from expanding down the density gradient because the stellar wind is strong enough that the contact discontinuity between the shocked wind and the swept-up material is

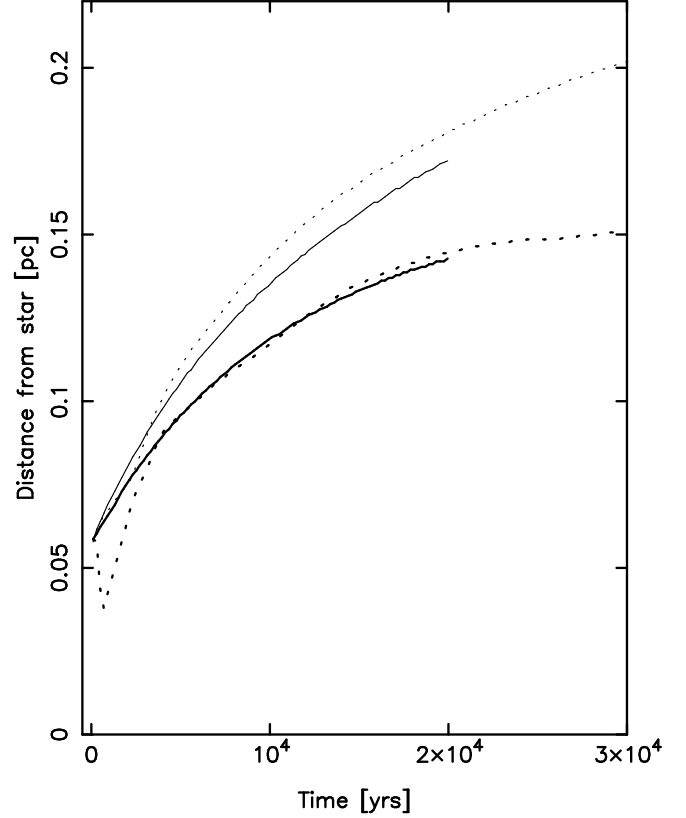


FIG. 6.— Distance from star of ionization front propagating up the density gradient against time for a champagne flow (thick solid line) and a champagne flow plus stellar wind (thick dotted line). Also plotted are the positions of the respective shock fronts in the neutral material ahead of the ionization front: thin solid line—champagne flow, thin dotted line—champagne flow plus stellar wind.

pushed past the position where the champagne flow would go through a sonic point (see, e.g., case A of Henney et al. 2005) and so the champagne flow stays subsonic on the axis. The champagne flow first establishes itself off-axis, where the advancing ionization front opens up and distances itself from the contact discontinuity, allowing the flow to become supersonic. The opening up of the ionization front appears to be driven by Kelvin-Helmholtz instabilities, which form at the head and travel down the structure, broadening as they reach regions of lower density and pressure. This leads to variations in the opacity and allows the ionization front to expand. Even though the external shock in Model C is the stellar wind shock, rather than the ionization front shock of Model A, the shock velocity is so small (see Figure 6) that the density enhancement is negligible and so the ionization front in Models A and C follows the same trajectory. The majority of the opacity in this part of the H II region comes from just behind the ionization front, since this is where the densest gas is to be found, hence even though the stellar wind has evacuated a cavity behind the ionization front, the conditions in the photoionized gas behind the ionization front are almost the same as in the pure champagne flow case and so the expansion is the same.

In Model B, at very early times, the shadowing instability is important (not shown here) and is triggered by a cooling instability in the swept-up thin shell (as discussed in § 2.2.2), which produces shadowing clumps. At the base of the spokes of ionized gas, the gas pressure widens the “gap” in the shell



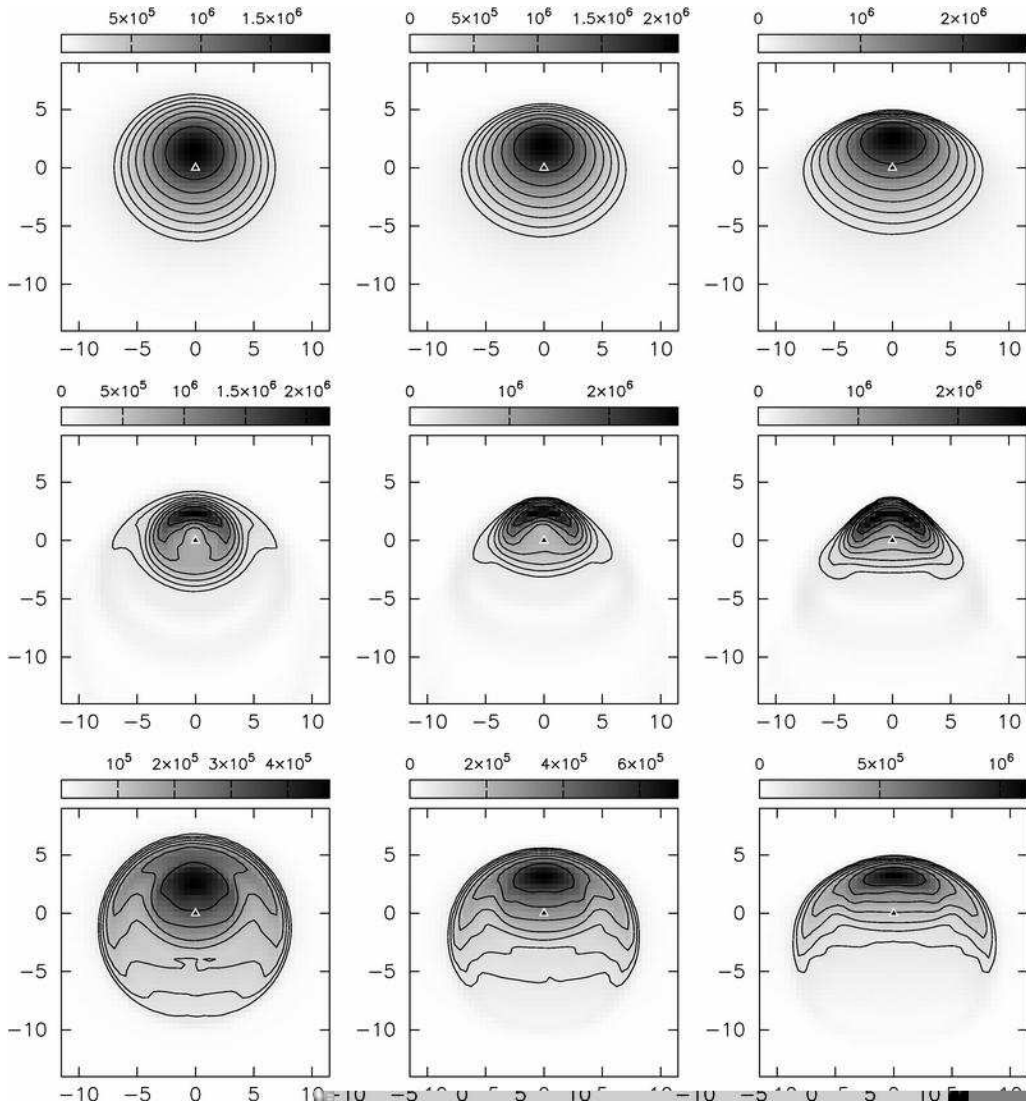


FIG. 7.— Linear greyscale and logarithmic contours with  $\sqrt{2}$  interval of the emission measure (units  $\text{pc cm}^{-6}$ ) for Models A (top), B (center) and C (bottom) at different projection angles after 20,000 years of evolution. For each row: left panel—projection angle  $30^\circ$ , center panel—projection angle  $45^\circ$ , right panel—projection angle  $60^\circ$ . The scale for each panel is given in arcsec. The position of the star is marked by a black triangle in each figure.

and allows the shocked stellar wind to flow through. This can be seen in the top panel Figure 4 as “ears” on the bowshock structure. Although strong advection around the bowshock after  $t > 10,000$  yrs leads to the disappearance of the characteristic spokes of ionized gas, the initial instability is the seed for a very turbulent interface between the hot, shocked stellar wind and swept-up material. This turbulent interface leads to the shedding of large eddies from the head of the bowshock and affects the thickness of the trapped ionized region. The eddies contain large amounts of dense, ionized material. At later times, Kelvin-Helmholtz instabilities at the interface region seem to be the dominant instability (cf. Raga et al. 1997; Comerón & Kaper 1998). The time sequence of images shown in Figure 4 shows that the shape of the bowshock varies considerably. At 10,000 yrs the shell is very thin, but with a large bowshock opening angle, at 20,000 yrs the shell is thin at the head but thicker at the sides, with a narrow bowshock opening angle, while at 40,000 yrs, the shell is quite thick and the opening angle of the bowshock is also quite large. The dense “blobs” on the axis in the 20,000 yrs figure are a result

of the imposed cylindrical symmetry focussing the turbulent flow onto the symmetry axis. Raga et al. (1997) state that, for late times of their models of high-velocity runaway O stars in low-density media, the bowshock flow reaches a “statistically stationary” regime. Our models have yet to achieve this regime but it could be expected that they will, since by 40,000 yrs all the transient features due to the initial instabilities have been advected a long way downstream. The eddies that are shed periodically from the apex of the bowshock cause pressure variations that alternately pinch then open up the region of shocked stellar wind.

The velocity fields in these models are quite complex. The photoevaporated flows in the champagne models (A and C) start at low velocities at the ionization front ( $v \sim 5 \text{ km s}^{-1}$ , see case A of Henney et al. (2005)) and are initially accelerated rapidly to the sound speed ( $v \sim 10 \text{ km s}^{-1}$ ), and then more gradually due to the density gradient, reaching velocities of around  $v \approx 30 \text{ km s}^{-1}$  before leaving the numerical grid (this gas would be below the detection limit due to its low density). In Model C, with a stellar wind, we also see thin shell insta-

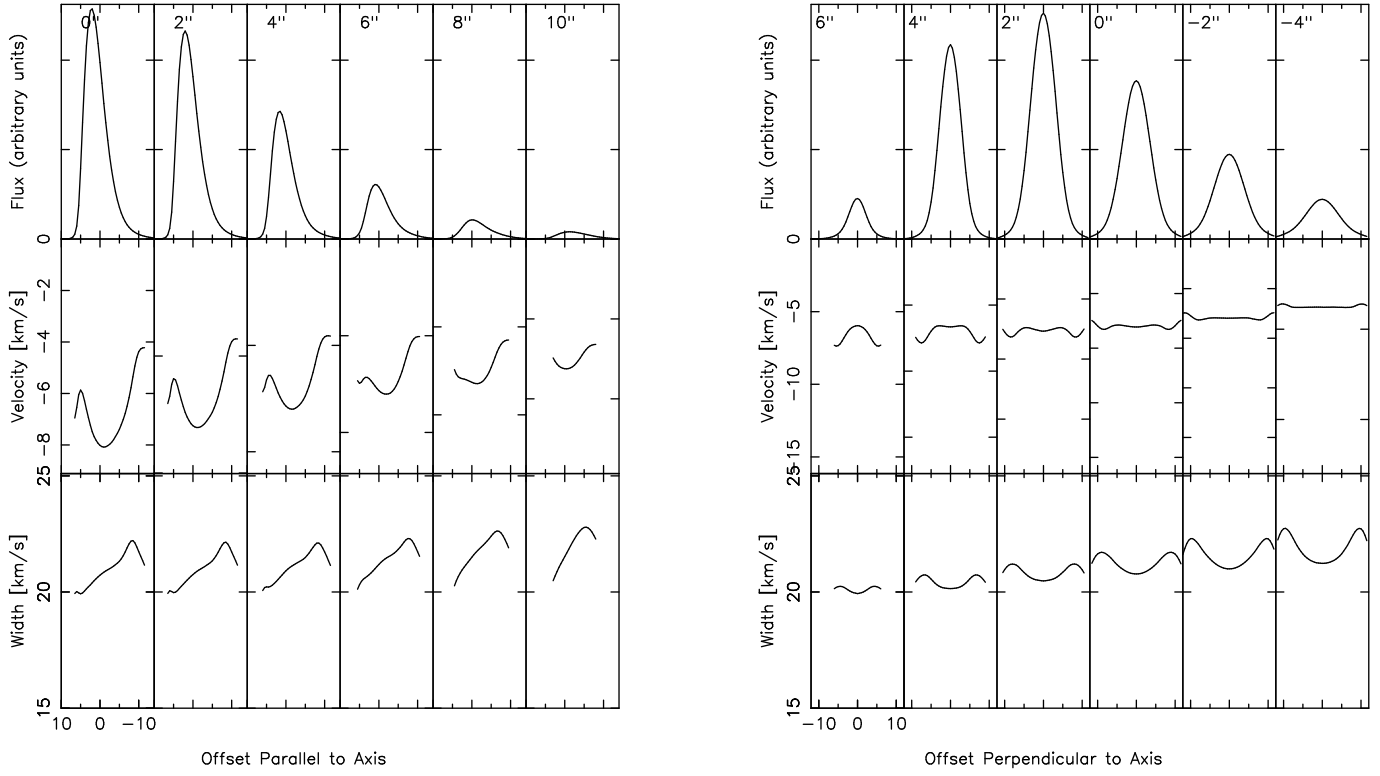


Fig. 8.— Simulated emission line moments for Model A (simple champagne flow), inclination angle  $45^\circ$ —line intensity, mean velocity and RMS velocity width (multiplied by scale factor  $2\sqrt{2\log 2}$ ) as a function of position along the slit. Left: slits parallel to symmetry axis; Right: slits perpendicular to symmetry axis. The offsets of the slits from the star are indicated in the upper left corner.

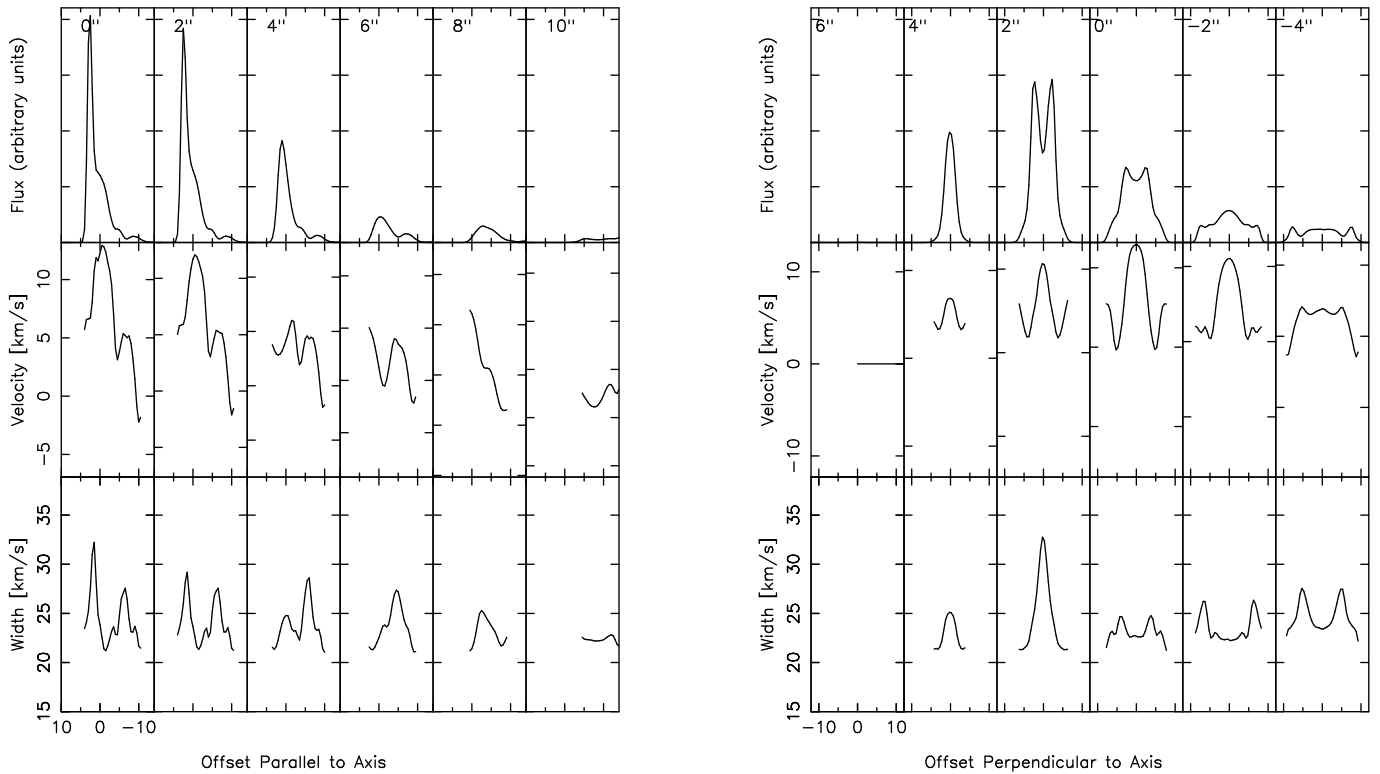


Fig. 9.— Same as Fig. 8 but for Model B ( $20 \text{ km s}^{-1}$  bowshock).

bilities, which form first in the densest part at the head of the cometary-shaped thin shell (because of faster cooling here) and later round the sides. The resulting knots are then deformed both by advection within the swept-up shell and also by Kelvin-Helmholtz instabilities due to the shear between the shell flow and the photoevaporated flow. Large knots of dense ionized material formed at the head of the cometary flow can thus be advected off the grid during the simulation timescale.

In the bowshock case (Model B), velocities at the head are roughly equal to the stellar velocity. Towards the tail of the cometary H II region, velocities in the dense, ionized gas are low and randomly oriented due to eddies formed at the shear interface. Although the highest velocities are to be found in the stellar wind itself, this gas has such low density that it is not detectable.

### 3.2.2. Simulated emission measure maps

Figure 7 shows the simulated emission measure smoothed by a Gaussian beam of  $1.0''$ . The numerical grid was projected onto a pixel grid whose longest dimension of 80 pixels represents a spatial size of  $2R \cos i + Z \sin i$ , where  $R$  and  $Z$  are the maximum extents of the radial,  $r$ , and longitudinal,  $z$ , directions of the numerical model (see e.g., Figure 3), and  $i$  is the inclination angle to the line of sight. In Figure 7 we have arbitrarily assigned an angular size of  $40''$  to be equivalent to 80 pixels. This would place all Models A and C at distances of approximately 7 kpc, depending slightly on inclination angle, while Model B would be at approximately 6 kpc. In Figure 7 we plot only a  $24'' \times 24''$  subset, with the projected stellar position assigned to  $(0, 0)$  in each case. For reasons of space, we show results only for inclination angles  $i = 30^\circ, 45^\circ$  and  $60^\circ$ . Emission measure maps for other inclination angles are available from the authors on request.

The emission measure maps show a range of morphologies. Model A (champagne flow) gives a clump or fan-shaped emission, as expected, while the addition of a stellar wind (Model C) flattens this emission and gives a more arc-like appearance. The bowshock model (Model B) results in an arc of limb-brightened emission, as expected.

### 3.2.3. Simulated spectra

In Figures 8–10 we plot the line intensity, mean velocity and velocity dispersion for slits parallel and perpendicular to the symmetry axis for the models shown in Figure 7 for inclination angle  $45^\circ$ . Results for other angles are available from the authors on request. These quantities are evaluated using the emission line moments, where the velocity dispersion is the RMS width scaled by a factor  $2\sqrt{2 \log 2}$ , which would give the FWHM in the case of a Gaussian profile. In each case the slit width is one arcsec and we have included thermal broadening using the temperatures which result from the numerical simulation. In the gas in photoionization equilibrium this temperature is  $10^4$  K but the partially ionized gas (either recently photoionized or in the process of recombining) will be at a lower temperature, and gas in the ionized, shocked stellar wind will be at a much higher temperature. The flux intensity for each slit is relative to the maximum intensity of the whole object. The slit offsets indicated are relative to the symmetry axis (for the parallel slits) and stellar position (perpendicular slits).

The peak flux intensity occurs on the symmetry axis ahead of the star. For the slits parallel to the symmetry axis, the flux intensity decreases steeply along the slit for all models. For

the slits perpendicular to the symmetry axis, there are differences between Models A, B, and C. For Model A (champagne flow), the peak flux in each slit always occurs on the symmetry axis and falls off to the sides. For Models B (bowshock) and C (champagne flow plus wind), the flux intensity has a flat-topped shape as the slits move down the tail of the cometary H II region, with peaks at the sides due to the emitting mass being concentrated in a shell around the low-density stellar wind bubble.

The velocity structures of Models A, B, and C are very different. In Figure 8 we see that the flow in Model A leaves the head of the cometary H II region with blueshifted velocities. It then accelerates and reaches maximum (blueshifted) speed at the projected position of the star. Thereafter, the velocities become more redshifted because of the contribution from the higher density, lower velocity, redshifted gas on the other side of the object in projection.

In Figure 9 (Model B) the velocities at the head are redshifted and correspond to the bowshock region being pushed forward ahead of the moving star. The noisiness of this spectrum is due to the eddies that form in the shear flow interface between the shocked stellar wind and the swept-up ambient medium. The drop in velocity just ahead of the projected position of the star in the slits parallel to the symmetry axis is because the line-of-sight cuts through a large region of low-density, low-random-velocity gas as well as through the more ordered, high blue-shifted velocity, dense material in the swept-up shell in the bow region. The velocities fall off steeply towards the tail region because the influence of the stellar motion on the gas is very small by this point.

Figure 10 (Model C) shows a combination of blue-shifted and red-shifted material. As for the simple champagne flow (Model A), the photoevaporated flow leaving the ionization front is blue-shifted. However, the stellar wind confines the champagne flow into a shell, causing it to flow around the stellar wind bubble. The line of sight through the shell at offset  $\sim -7''$  cuts through a thick, dense region of redshifted velocities, which weight the spectrum and lead it to turn over.

The velocity widths of Model A increase from head to tail of the champagne flow but are uniform across it for a given slit, and do not differ much from the value of the thermal width. In Model B, the velocity widths are noisy for slits parallel to the symmetry axis, due to the eddies formed in the shear flow. The widths of Model C increase towards the wings of the cometary H II region, due to the ionized gas being channeled into a shell and accelerated around the stellar wind zone.

Although we do not show them here, the spectra for Models B and C at 40,000 yrs are very similar to those at 20,000 yrs, particularly as regards the velocity range and pattern. There are differences in the line widths, with the widths after 40,000 yrs being generally smoother, reflecting the fact that eddies formed earlier in the simulation at the head of the object are advected down the structure where they expand and so their influence diminishes.

## 4. MODIFIED MODELS

Taking Models A, B, and C as our reference models, we vary parameters such as the stellar wind strength and the density scale height to examine their effect on the morphology and kinematics of the resultant cometary H II regions. We also study the effect of stellar motion up a density gradient, considering stellar speeds of 5 and 10 km s<sup>-1</sup>. The parameter space to explore is huge, and we restrict ourselves to a few

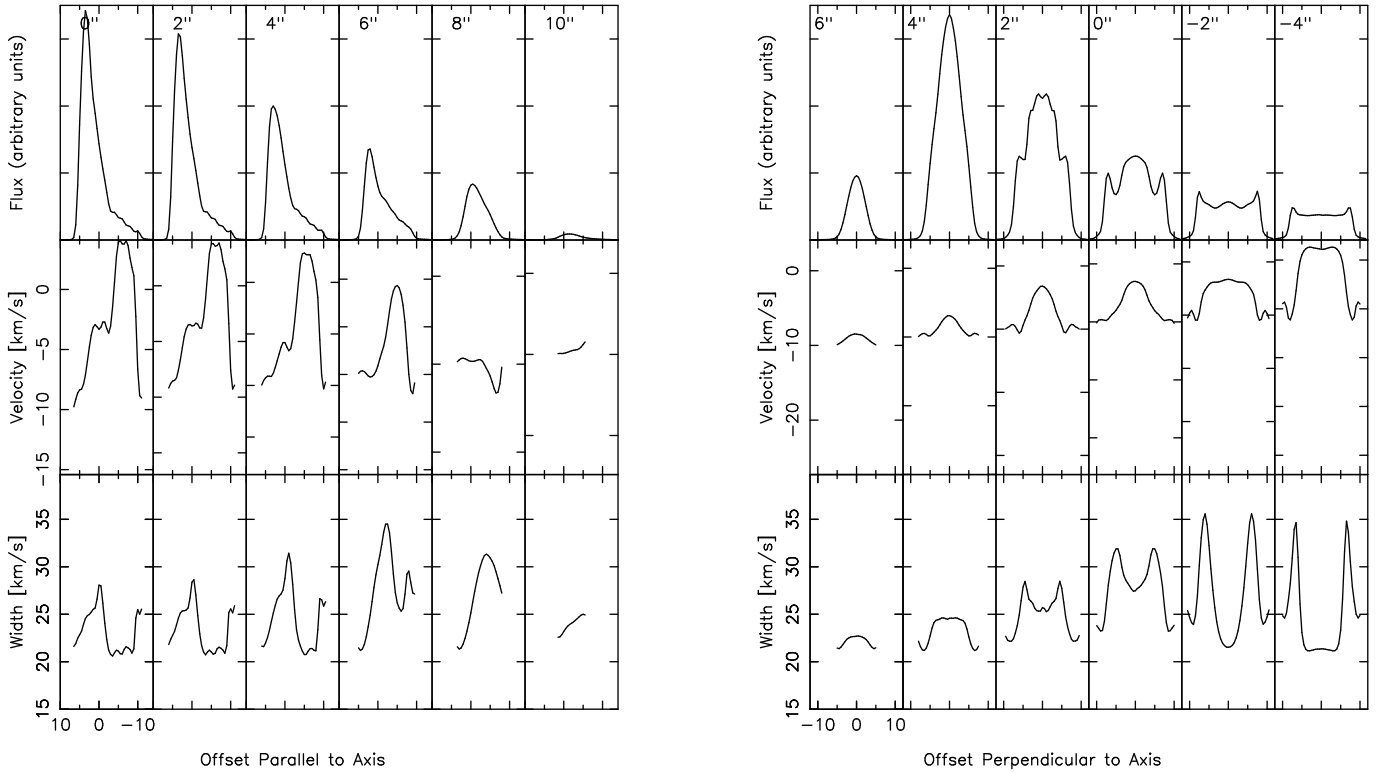


FIG. 10.— Same as Fig. 8 but for Model C (champagne flow plus stellar wind).

representative cases.

#### 4.1. Model parameters

##### 4.1.1. Champagne flow plus stellar wind: Models D, E, and F

These models are similar to Model C, except that in Model D the stellar wind mass loss rate is an order of magnitude smaller,  $\dot{M} = 10^{-7} M_{\odot} \text{ yr}^{-1}$ , in Model E the scale height of the density distribution is much larger,  $H = 0.2$  parsec, and hence the density gradient is shallower. In Model F the density distribution is spherical, rather than plane parallel, and is given by

$$n = n_0 \left[ 1 + \left( \frac{R}{r_c} \right)^2 \right]^{-\alpha} \quad (2)$$

where  $n_0 = 9.8 \times 10^6 \text{ cm}^{-3}$  is the number density at the center of the core of this distribution, where the core is assumed to have a radius  $r_c = 0.01$  pc, and  $R^2 = r^2 + z^2$  is the spherical radius. The exponent  $\alpha = 1$  in this model, giving  $n \propto R^{-2}$  at large radii. The star is offset from the center of the distribution such that  $n = 8000 \text{ cm}^{-3}$  at its position.

##### 4.1.2. Champagne flow plus stellar wind plus stellar motion: Models G, H, and I

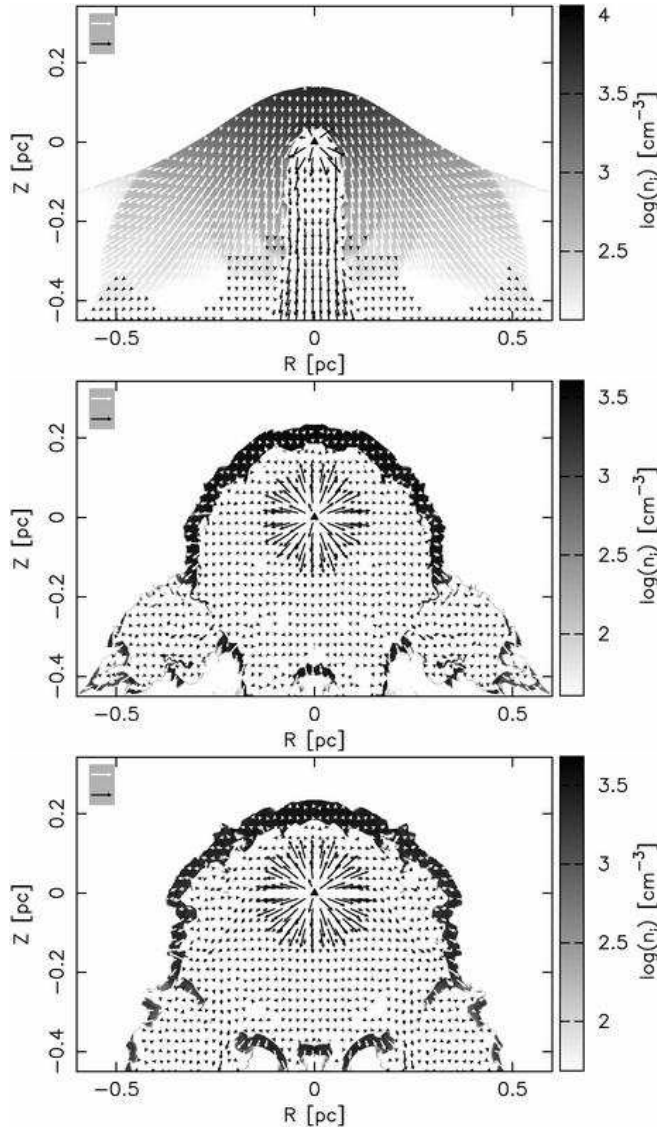
These models combine a density gradient, stellar wind and stellar motion. Models G and H have an exponential density distribution with scale height  $H = 0.05$  parsec. In Model G the star's velocity is  $5 \text{ km s}^{-1}$  and the star starts from  $0.05$  pc below the position where the number density is  $n = 8000 \text{ cm}^{-3}$ , while for Model H the velocity is  $10 \text{ km s}^{-1}$  and the star starts from  $0.1$  pc below this reference position. Finally, Model I also has an exponential density distribution

but with a larger scale height,  $H = 0.2$  pc and the star's velocity is  $V_* = 10 \text{ km s}^{-1}$ , where the star again starts its motion a distance  $0.1$  pc below the position where the number density is  $n = 8000 \text{ cm}^{-3}$ .

#### 4.2. Modified model results

##### 4.2.1. Velocity field

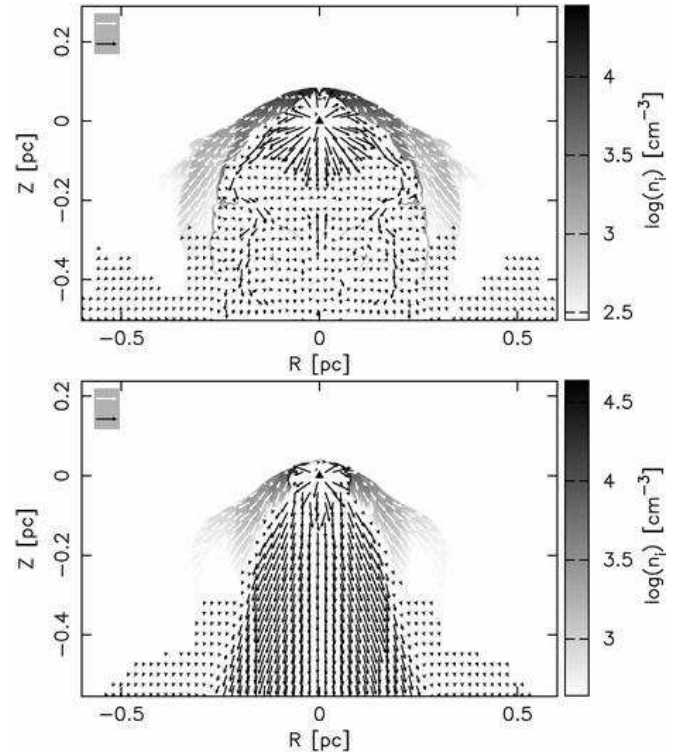
Figure 11 shows the ionized density (greyscale) and velocity field in the  $r - z$  plane for Models D, E and F of Table 1 after 20,000 yrs of evolution. Model D looks very similar to a champagne flow, with the stellar wind only affecting a narrow region deep within the ionized zone. Models E and F are both cases of a champagne flow in a shallow density distribution. In these cases, the stellar wind can reach pressure balance with the external medium within a scale height and the inner wind shock is almost spherical. The shocked stellar wind region is also approximately spherical, except for in the tail region where it has broken out into the lower density surroundings. At the head of the cometary H II region there is a thick shell of ionized gas flowing off the ionization front, which is then diverted around the outside of the stellar wind bubble. Because the ambient density does not fall off very quickly, the density in the ionized gas shell is high and fairly uniform, and the ionization front becomes trapped in the shell, unlike in Model C, where the rapid fall-off in density means that the ionization front can break through the swept-up shell in the tail. In Models E and F the shallow density gradient allows the shadowing instability to form broad spokes in the lowest density gas, where the pressure at the base of the spokes opens gaps in the swept-up shell through which the shocked stellar wind can flow. This can be seen clearly in the corresponding panels of Figure 11.



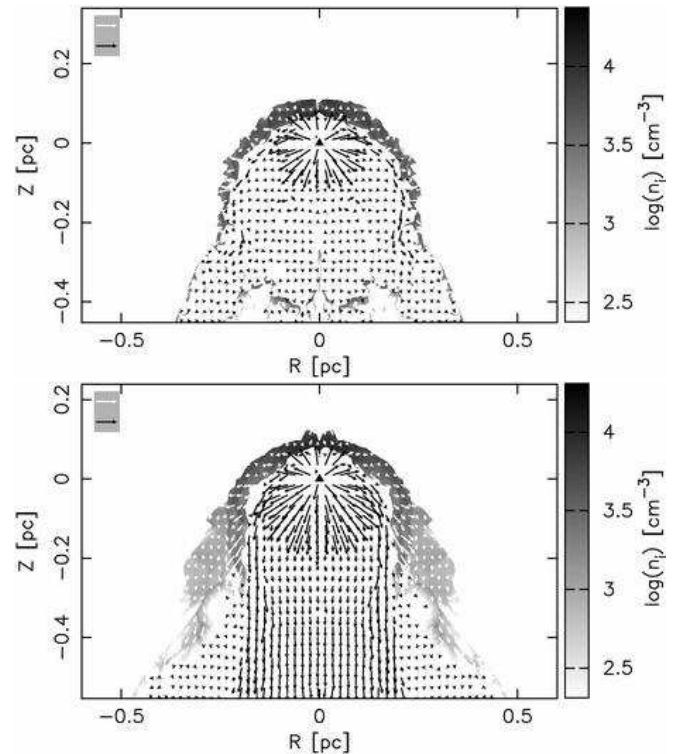
F . 11.— Same as Fig. 4 but for models (from top to bottom) (a) Model D: champagne flow plus stellar wind,  $H = 0.05$  pc,  $\dot{M} = 10^{-7} M_{\odot} \text{ yr}^{-1}$  (b) Model E: champagne flow plus stellar wind,  $H = 0.2$  pc,  $\dot{M} = 10^{-6} M_{\odot} \text{ yr}^{-1}$  (c) Model F: champagne flow, spherical density distribution. All models shown after 20,000 years of evolution.

The velocities in Model D are very similar to the simple champagne flow model. In Models E and F the velocities in the ionized shell are fairly low and there are some turbulent regions due to instabilities which are slowly being advected down the shallow density gradient.

Figures 12 and 13 show the ionized density and velocity fields for Models G, H, and I. Model I has the shallowest density gradient and this is reflected in its more spherical, thicker, ionized shell. There is a lower emission measure region outside of the main shell. Models G and H have the same steep density gradient. Both of these models show a champagne flow as well as a stellar wind swept-up shell. The stellar velocity in Model G is half that of Model H and this results in the photoionized shell ahead of the star in Model G being thicker than that in Model H. In Figure 12, the star in Model H has reached a denser part of the ambient density distribution than the star in Model G but comparing the two models when the



F . 12.— Same as Figure 4 but for models with density gradient plus stellar wind plus stellar motion. (a) Top—Model G:  $V_{*} = 5$  km  $\text{ s}^{-1}$ ,  $H = 0.05$  parsec. (b) Bottom—Model H:  $V_{*} = 10$  km  $\text{ s}^{-1}$ ,  $H = 0.05$  parsec. Both models shown after 20,000 yrs of evolution.



F . 13.— Same as Figure 4 but for models with density gradient plus stellar wind plus stellar motion (from top to bottom) (a) Model I:  $V_{*} = 10$  km  $\text{ s}^{-1}$ ,  $H = 0.2$  parsec after 10,000 yrs (b) Model I' after 20,000 yrs of evolution.

star is at the same position still shows that the photoionized shell ahead of the star in Model H is thinner. Also, the hot, shocked stellar wind in Model G occupies a greater fraction of the volume than in Model H. In fact, in the tail of Model H, the stellar wind does not go through a global decelerating shock as in Model G, but instead appears to have an oblique shock surface that neither heats nor decelerates the wind very much. In Model I, the stellar wind suffers a global decelerating shock but then in the downstream direction is focussed by the ionized shell and reaccelerated by a nozzle effect.

The velocity fields of Models G, H, and I show that large accelerations can occur around the sides of the flow in the ionized gas, with velocities reaching  $30 \text{ km s}^{-1}$  or more. This is an effect of including a density gradient, since in a simple bowshock model there is no acceleration around the sides and velocities fall off quickly towards the tail. Models G and H show the largest accelerations towards the tails of the champagne flows, and this is entirely consistent with them having the steepest density gradient. In Model I, the highest velocities occur in the swept up shell as it expands into the low density region. Ahead of the star, the velocities at the ionization front in these three models are low (i.e., lower than the stellar velocities) and in the direction of stellar motion, unlike the stationary star cases.

In these models, the shadowing instability only occurs at the earliest times and is most noticeable in Models G (due to the low stellar velocity) and I (due to the shallow density gradient). In both cases the instability soon disappears ( $t < 3000 \text{ yrs}$ ) because of advection of the shadowing clumps around the shell. At later times the dominant instabilities are Rayleigh-Taylor and Kelvin-Helmholtz type due to the shear between the champagne flow and the shocked stellar wind flow.

#### 4.2.2. Emission measure maps

In Figure 14 we show the emission measure maps at projection angles of  $i = 30^\circ, 45^\circ$  and  $60^\circ$  for models D, E, and F. (Emission measure maps for other inclination angles are available from the authors.) Model D closely resembles the emission measure one expects from a pure champagne flow, since the stellar wind is not strong enough ( $\dot{M} = 10^{-7} M_\odot \text{ yr}^{-1}$ ) to confine the photoevaporation flow from the ionization front. Subtle evidence of the wind interaction can be seen in the contours. There is a lack of emission on the axis and a faint brightening corresponding to the shell formed by the interaction between the wind and the champagne flow.

Models E and F are examples of champagne flows with stellar winds in shallow density gradients. In these cases, the stellar wind is strong enough ( $\dot{M} = 10^{-6} M_\odot \text{ yr}^{-1}$ ) to confine the photoevaporated flow to a thick shell and the resultant emission measure maps show an arclike rather than fan-like morphology. The shallow density gradient in these models means that the emission measure does not fall off very quickly towards the tail of the H II region and so they appear more shell-like (see, e.g., De Pree et al. 2005). Models G, H, and I all show limb-brightened emission measure maps (Fig. 15), with the limb-brightening being most enhanced for the largest angle to the line of sight ( $i = 60^\circ$ ). Model I, having the shallowest density gradient, has a “filled shell” type morphology, whereas Models G and H are arclike. In Model H the arc of most intense emission is situated much closer to the star than in the other models, principally because the star has reached denser gas than in Models G and I. The ionized shell in Model H (see Figure 12) is much thinner than in Models G

and I and this is reflected in the steep drop-off in intensity both ahead and behind the emission peak.

#### 4.2.3. Simulated spectra

The spectra of Model D shown in Figure 16 do not differ too much from the standard champagne flow spectra (Model A). In the spectrum of Model E (Fig. 17) the flux does not fall off so fast with distance from the head of the cometary H II region since the density gradient is shallower. Knots in the swept-up wind shell cause features in the velocity plot, but otherwise line-of-sight velocities in the ionized gas are very low ( $< 5 \text{ km s}^{-1}$ ). The density gradient has little effect on the dynamics because it is so shallow and the swept-up shell of ambient material is neither expanding very rapidly nor has important transverse motions. The spectrum of Model F (Fig. 18) is very similar, although for offsets between  $-10''$  and  $-5''$  the flux, velocity and velocity widths are dominated by the broken shell which can be seen in Figure 11. This broken shell is a transient feature which will eventually be advected downstream. All the Models G, H, and I show blueshifted velocities at the head of the cometary H II region changing to redshifted velocities once the offset has passed the position of the star, as can be seen in Figures 19–21. Even though the ionized gas velocities ahead of the stars in these models are positive (i.e., in the direction of stellar motion), the projection angle gives more weight to the gas in the blue-shifted flow in the ionized shell and champagne flow at the nearside of the cometary H II region. The “noise” seen in these spectra is due to instabilities (eddies) moving through the ionized layer. Model I, having the shallowest density gradients, shows the smallest range of velocities ( $\sim 10 \text{ km s}^{-1}$ ), while models G and H show a range of  $\sim 15 \text{ km s}^{-1}$  even though the velocity of the star is only  $5 \text{ km s}^{-1}$  and  $10 \text{ km s}^{-1}$  respectively. This is mainly due to the champagne flow formed in the steep density gradient and is very similar to what is seen in the case of Model C (Fig. 10).

The velocity widths show varied behaviour. Model G achieves widths of  $\sim 40 \text{ km s}^{-1}$  in the wings of the tail. On the other hand, the highest widths  $\sim 30 \text{ km s}^{-1}$  of Model H are nearer the head. Model I displays a small range of velocity widths, which are also higher towards the head of the object. Some of the variation in the line widths is due to eddies being advected through the structure.

## 5. DISCUSSION

### 5.1. Champagne flow Model

From Figure 6 we can derive approximate empirical expansion laws for the ionization front and shock into the neutral material for the photoevaporated champagne flow (Model A) and champagne flow plus stellar wind (Model C) cases. We find that for times  $2 \times 10^3 < t < 2 \times 10^4 \text{ yrs}$  a good approximation to the ionization front velocity for both Models A and C is

$$v = 3.46 t_4^{-0.7} \text{ km s}^{-1}, \quad (3)$$

while the shock front expansion for the same temporal range for Model A can be approximated by

$$v = 4.75 t_4^{-0.64} \text{ km s}^{-1}, \quad (4)$$

and for Model C by

$$v = 4.99 t_4^{-0.64} \text{ km s}^{-1}, \quad (5)$$

where  $t_4$  is the time,  $t/10^4 \text{ yrs}$ . If we work out the shock velocities for  $t = 2 \times 10^4 \text{ yrs}$ , we find  $v_s = 3.05 \text{ km s}^{-1}$

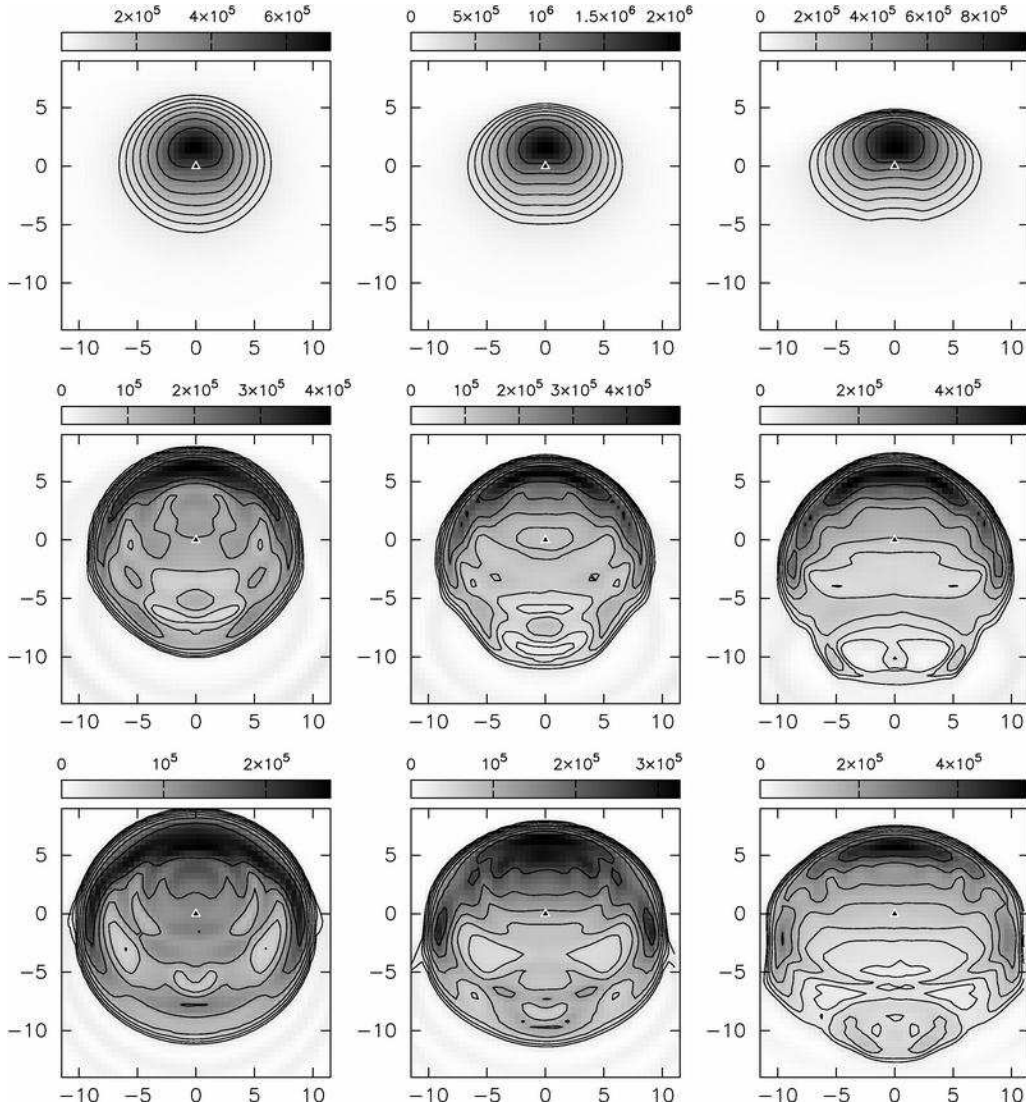


FIG. 14.— Same as Figure 7 but for Models D, E, and F after 20,000 years of evolution.

for Model A and  $v_s = 3.20 \text{ km s}^{-1}$  for Model C. The shock velocity for Model C is slightly faster than that of Model A because the stellar wind shock has overtaken the ionization front shock. Although these results are specific to the stellar wind parameters and density distribution (and time), they are broadly consistent with observations by Roshi et al. (2005) of carbon recombination lines towards the ultracompact H II region G35.20–1.74. These observations show velocities in the neutral gas in the PDR of  $2.5 \text{ km s}^{-1}$  into the cloud, while the ionized gas has velocities away from the cloud, as expected for a photoevaporated flow (see Henney et al. 2005, for a detailed discussion of the velocities of the different components associated with ionization fronts).

The ionization front velocity for both models at 20,000 yrs is  $2.13 \text{ km s}^{-1}$ . In these models, the front is almost D-critical and the ionized gas leaves the front at about half the sound speed ( $v \approx -5 \text{ km s}^{-1}$ ), passing through a sonic point ( $v \approx -10 \text{ km s}^{-1}$ ) by the time the ionization fraction becomes equal to unity (Henney et al. 2005). For more open (i.e., less concave) ionization fronts the gas leaves the front even faster and accelerates more rapidly to the sound speed. Hence

the net velocity of the ionized gas at the ionization front is  $\sim -3 \text{ km s}^{-1}$  in the rest frame of the cloud and becomes more blueshifted (in this scenario) as it flows away from the front. A popular misconception in the literature is that the velocities at the head of a champagne flow should be the same as those of the molecular cloud.

We note here that the analytic expressions for the shape of the ionization front in a strong density gradient derived by, for example, Icke et al. (1980) are not correct since they do not take into account the motion of the gas, which has the effect of flattening the density gradient. Thus, the density gradient in the quasi-stationary champagne flow is not the same as the much steeper density gradient in the ambient material. The density gradient within these analytic ionized regions has no physical basis. In our numerical models, however, the hydrodynamics and radiative transfer are solved simultaneously, giving a physical result.

The numerical champagne flow models of Tenorio-Tagle and collaborators (Tenorio-Tagle 1979; Bodenheimer et al. 1979; Bedijn & Tenorio-Tagle 1981; Yorke et al. 1983), and more recently by Comerón (1997) are for the different physi-

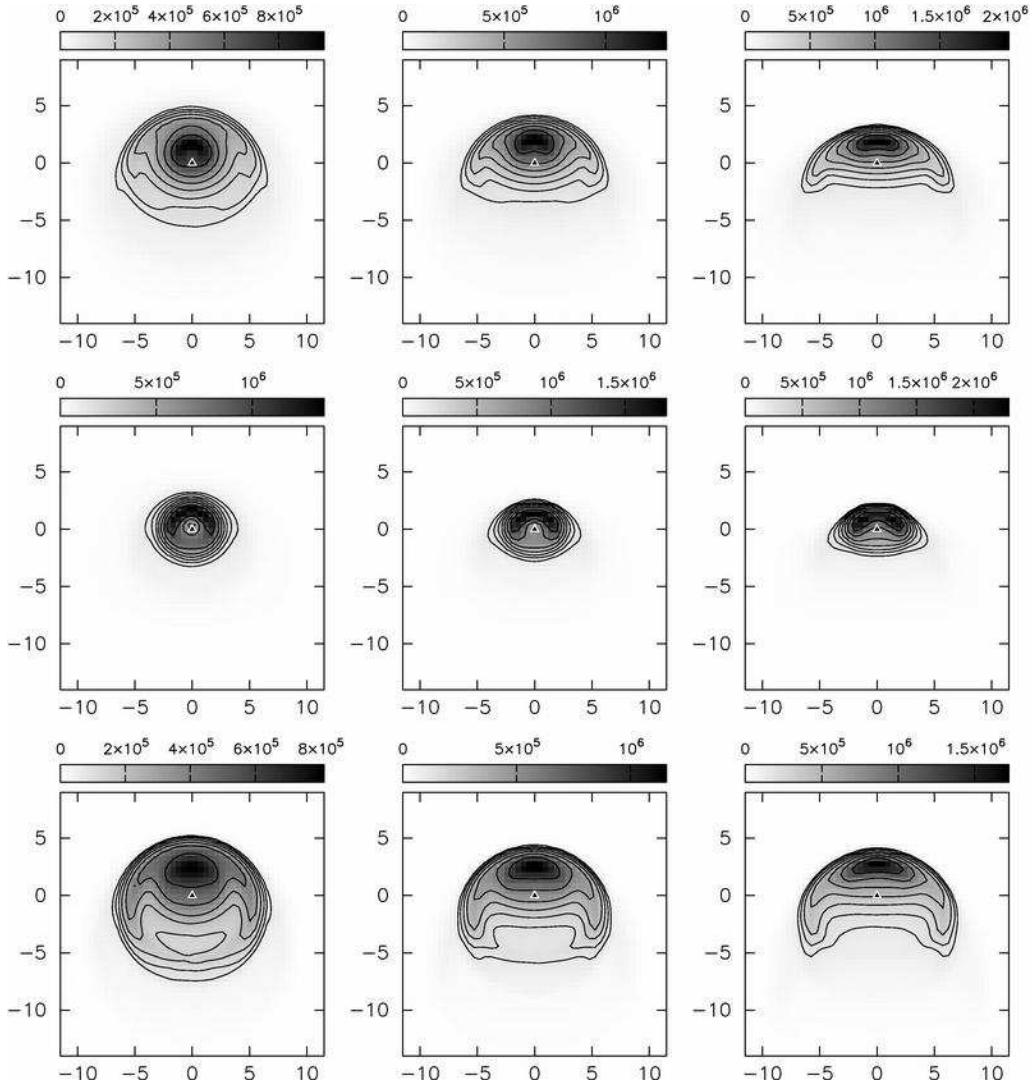


FIG. 15.— Same as Figure 7 but for Models G, H, and I after 20,000 years of evolution.

cal setup of a spherical H II region breaking out from a dense, uniform cloud into a diffuse intercloud medium, where the distance of the star from the sharp cloud/intercloud interface is a determining parameter for the resultant flow. We feel that a more realistic density distribution would not be discontinuous, as in the above papers, but would show a smoother transition between high cloud and low intercloud densities. Hydrodynamical simulations of the formation and expansion of H II regions in disk-like clouds with stratified density distributions were done by Franco et al. (1989) and Franco et al. (1990), but in these models the star is placed at the midplane, which is a special place. For this reason, these models do not give rise to photoevaporated champagne flows.

In the present work we adopted exponential density distributions with different scale heights. These distributions have the advantage that the density depends only on the height,  $z$ . We also investigated a spherical density distribution (Model F), where the density depends on both  $z$  and the cylindrical radius  $r$ . However, the results in this case are not qualitatively dissimilar from those of the exponential distribution with a large scale height (Model E). Models with large scale heights show the smallest departures from idealized H II

regions, while small scale heights produce the greatest differences.

### 5.2. Bowshock Model

In Figure 22 we compare our numerical results to the analytical solution found by Wilkin (1996) for stellar wind bowshocks in the thin-shell limit. The analytical solution for the shape of the bowshock is given by

$$r(\theta) = r_0 \csc \theta \sqrt{3(1 - \theta \cot \theta)} \quad (6)$$

where  $r_0 = (\dot{M}_w v_w / 4\pi \rho_a v_*^2)^{1/2}$  is the stand-off distance,  $\dot{M}_w$ ,  $v_w$  are the stellar wind mass loss rate and velocity respectively,  $\rho_a$  is the ambient density and  $v_*$  is the stellar velocity. The angle  $\theta$  is measured with respect to the star from the symmetry axis. This model assumes that both the shocked stellar wind and the swept-up shell of ambient material are thin, i.e., that cooling is efficient in both shocked zones. The shape of the bowshock should be compared to that of the contact discontinuity between the shocked stellar wind material and the swept-up ambient medium.

The numerical result differs from the analytical result for a variety of reasons. The main reason is that the key assumption



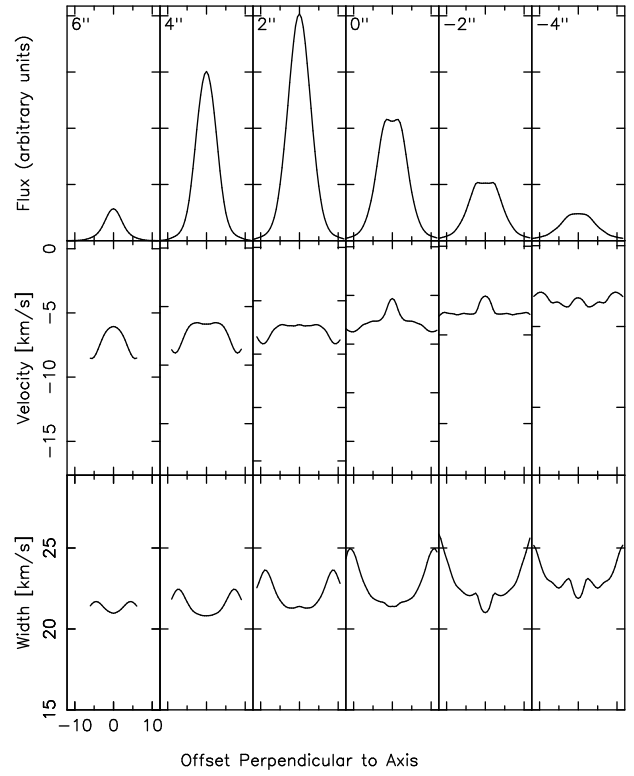
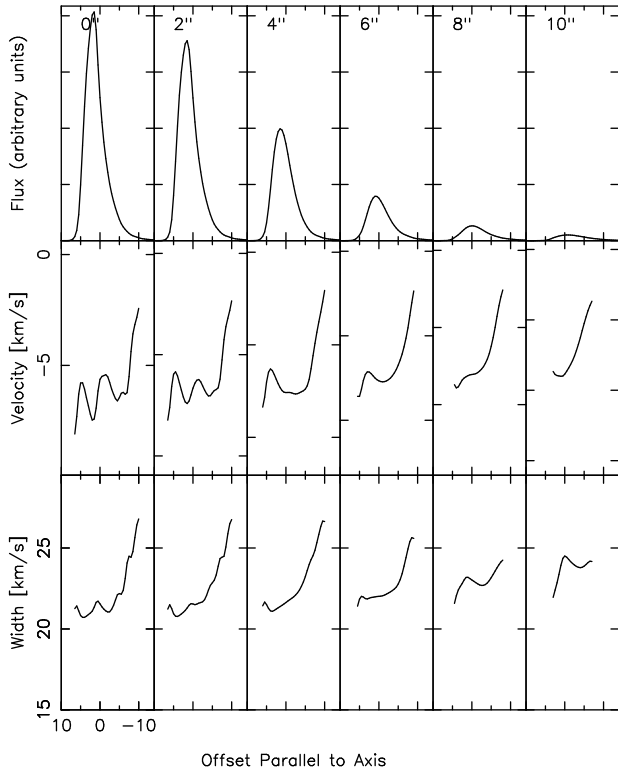


Figure 16.— Same as Fig. 8 but for Model D.

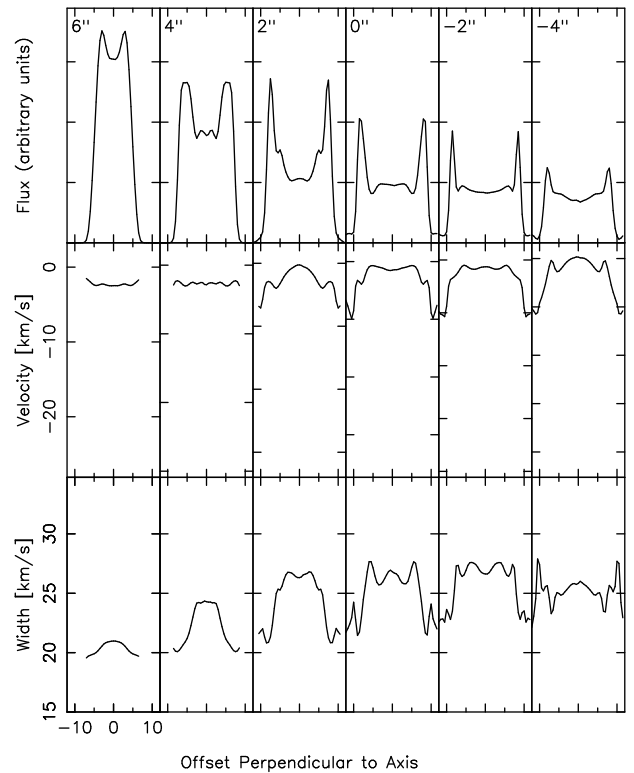
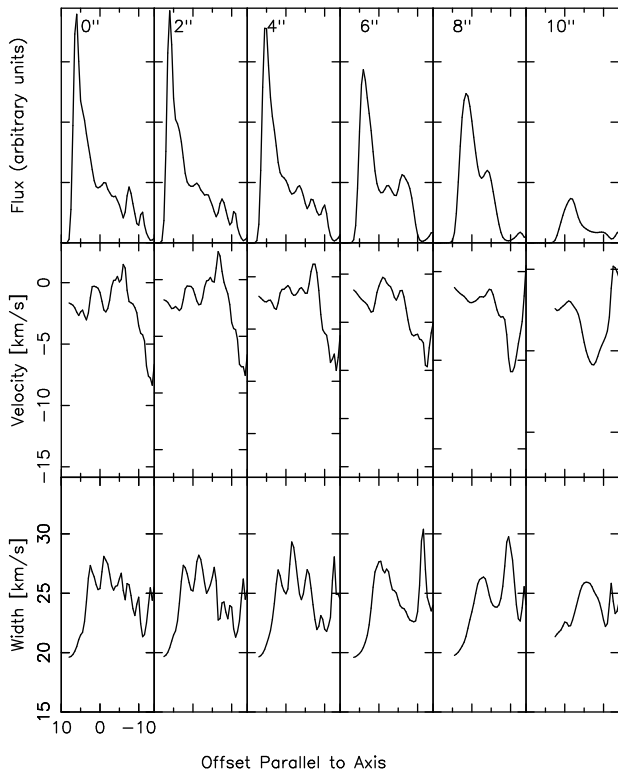
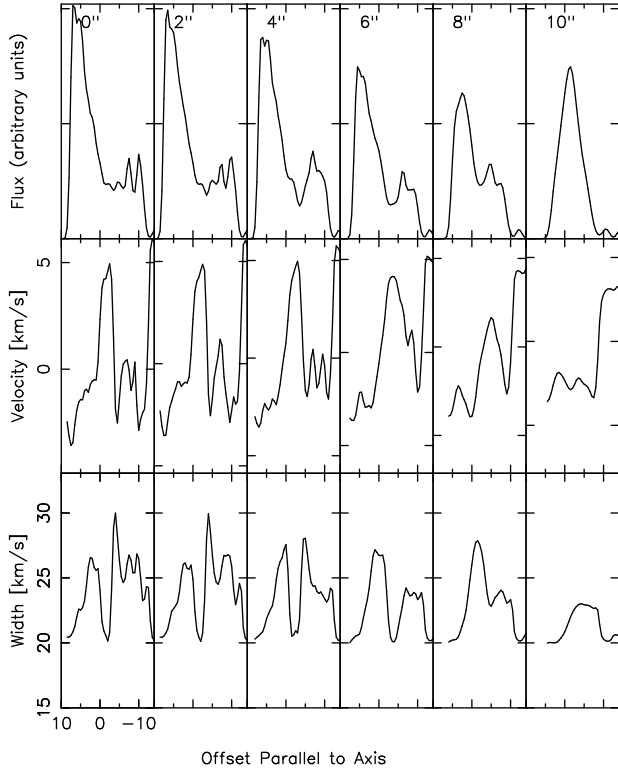
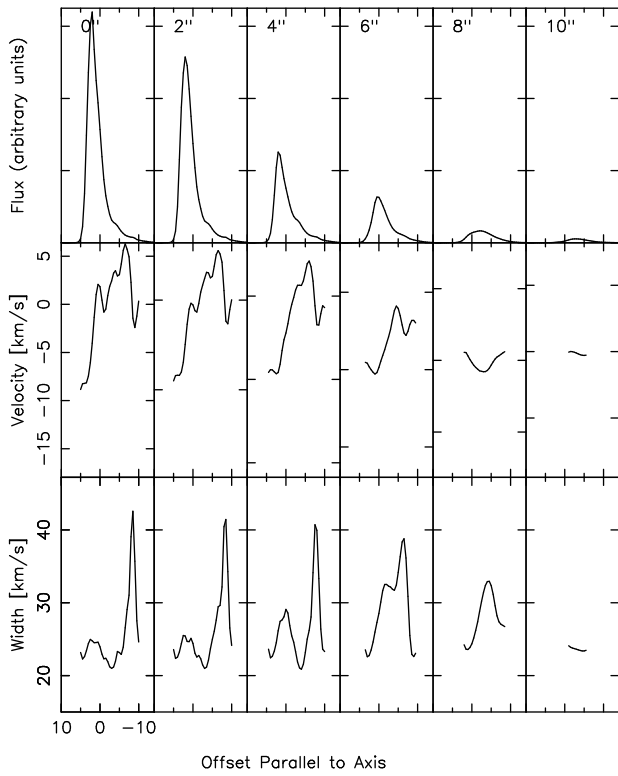
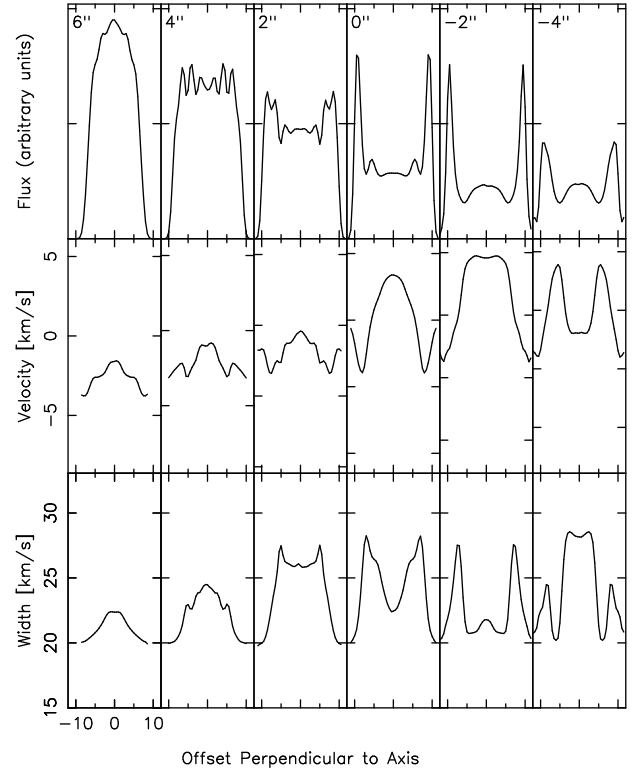


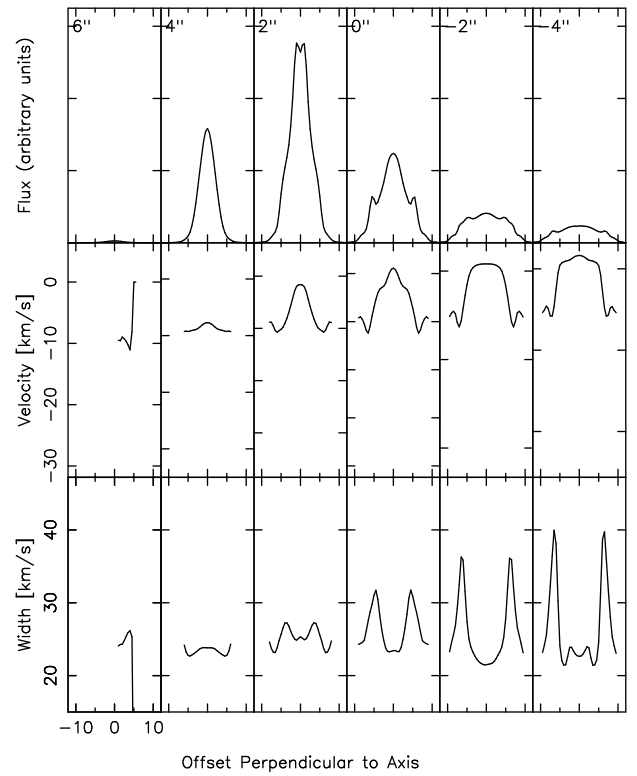
Figure 17.— Same as Fig. 8 but for Model E.



F . 18.— Same as Fig. 8 but for Model F.



F . 19.— Same as Fig. 8 but for Model G.



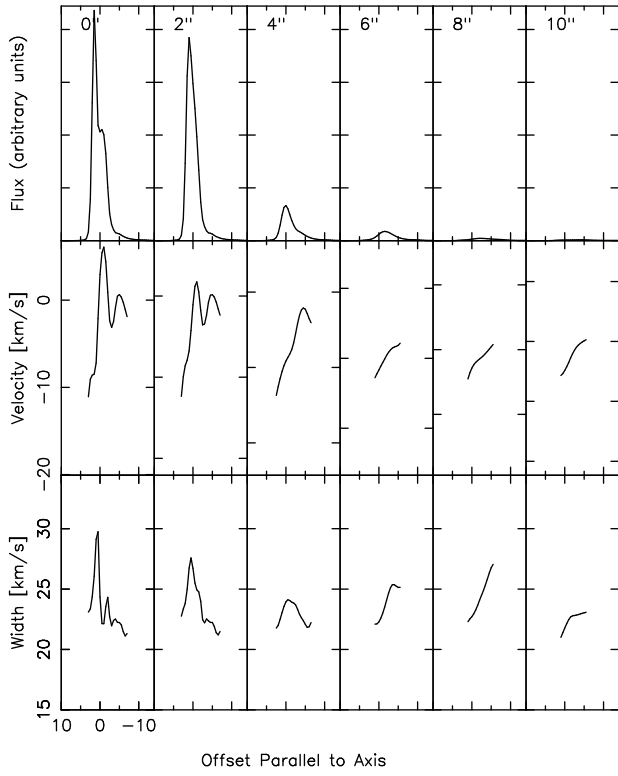


Figure 20.— Same as Fig. 8 but for Model H.

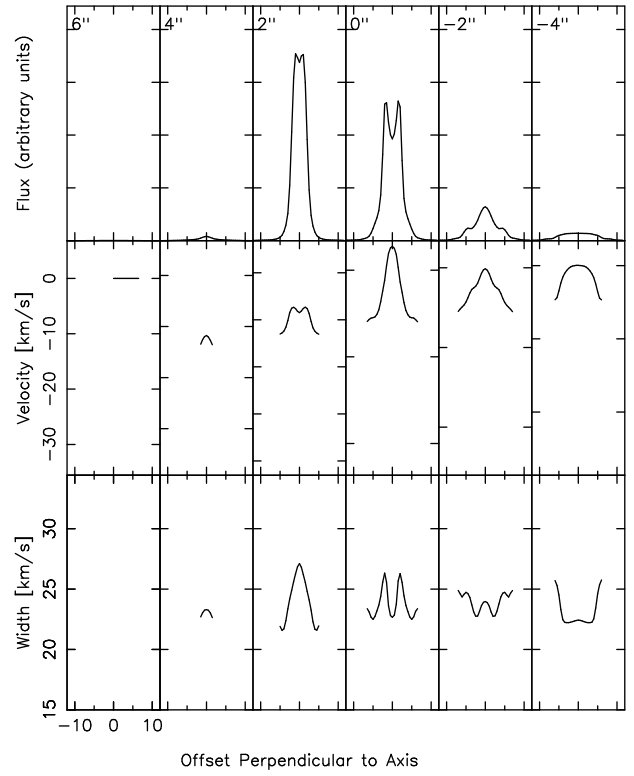


Figure 21.— Same as Fig. 8 but for Model I.

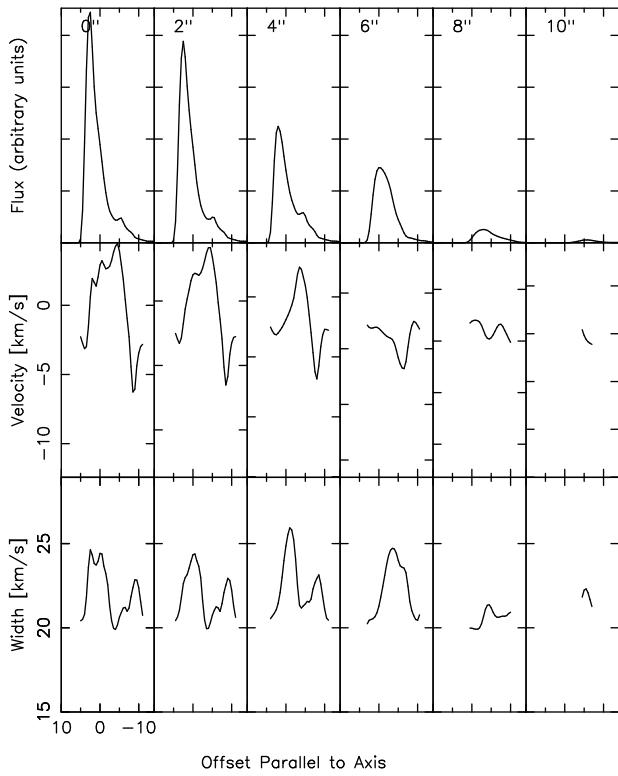


Figure 22.— Same as Fig. 8 but for Model H.

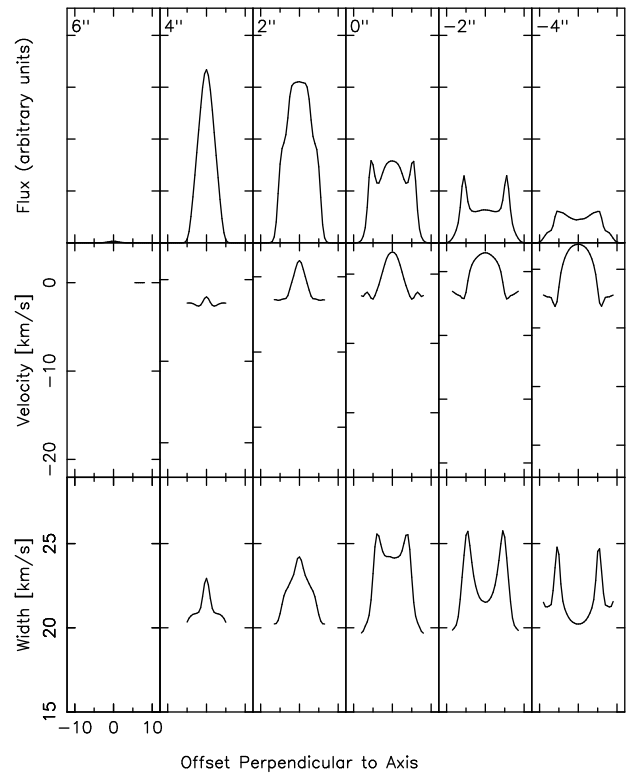


Figure 23.— Same as Fig. 8 but for Model I.

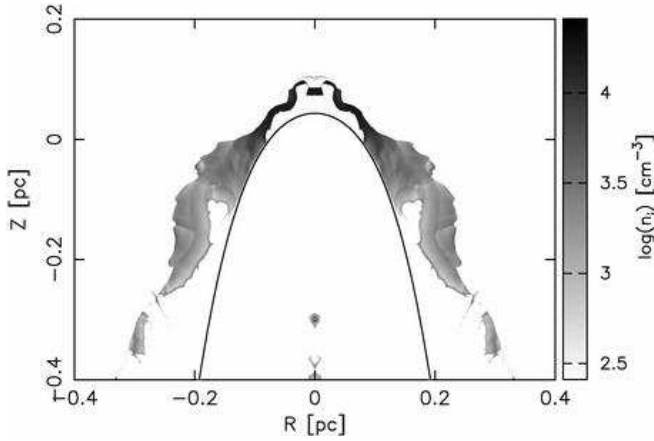


FIG. 22.— Logarithm of ionized number density for the simple bowshock model (Model B after 20,000 years of evolution) with the analytic solution for the shape of the thin shell from Wilkin (1996) overplotted.

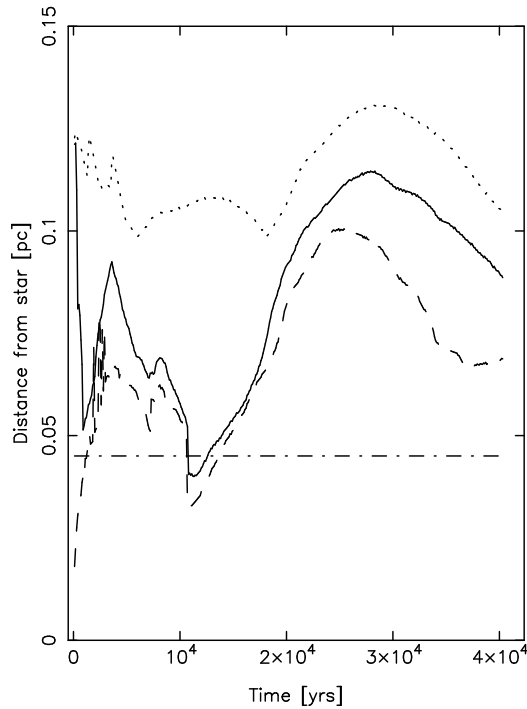


FIG. 23.— Distance of ionization front (solid line), stellar wind contact discontinuity (dashed line), and outer shock in neutral medium (dotted line) from the star as a function of time for the bowshock model (Model B). The dot-dashed horizontal line represents the position of ram-pressure balance between the stellar wind and the ambient medium at the apex of the bowshock formed by the moving star.

of the analytical result is that cooling in the shocked stellar wind is instantaneous, making this region thin. In the present models the stellar wind shocks and a region of high temperature forms between the free-flowing wind and the swept-up ambient medium. The thickness of this subsonic region varies as the evolution proceeds since pressure balance across the contact discontinuity means that it is sensitive to what is happening behind the outer shock.

Additionally, in the numerical model the ionizing photons and stellar wind switch on at the same time. Thus, a Strömgren sphere forms around the star almost instantaneously, while the stellar wind bubble takes much longer to

form. The stellar wind sweeps up a shell of material, which then cools on a timescale dependent on the postshock temperature and density. As the hydrodynamic flow develops, the initial photoionized region starts to expand, preceded by a shock wave, that sets the neutral gas ahead of the photoionized region in motion. It is into this moving medium that the stellar wind bubble expands. The impact of the hypersonic stellar wind on the surrounding medium sets up the familiar two shock pattern (Dyson & Williams 1997), where the outer shock sweeps up the ambient medium. This swept-up shell forms initially within the photoionized region. However, due to the increased opacity, the ionization front retreats until it is contained within the shell. At this point, the shock ahead of the original ionization front is still expanding into the ambient medium, although the previously ionized gas outside the shocked shell now recombines. The swept-up shell expands into this moving neutral gas and thickens. Instabilities are formed in the cooling shell, which lead to turbulent motions in the subsonic region between the outer shock and the inner stellar wind shock. The shell is initially thick, and only starts to become thinner once the outer stellar wind shock has overtaken the shock produced by the initial ionization front. The ionization front moves outwards within the stellar wind shell and the pressure of the photoionized gas is an additional confinement on the shocked stellar wind. Pressure gradients across the bowshock structure and transverse to it mean that the ram pressure balance across thin shells is inadequate to describe the evolution of the structure at these early times ( $t < 40,000$  yrs).

In Figure 23 the distance of the ionization front and stellar wind contact discontinuity and the outer shock in the frame of the star are plotted for the bowshock model. We also indicate in this figure the position of theoretical ram pressure balance. In this figure we see how the initial ionization front retreats into the swept-up shell, while the shock that was sent out into the neutral gas travels for quite a time at roughly the stellar velocity ( $20 \text{ km s}^{-1}$ ) before being finally overtaken by the outer stellar wind shock. Once the ionization front is trapped in the shell, it remains there for the rest of the evolution. The noise in the position of the contact discontinuity occurs when instabilities form in the subsonic region between the shocks. The first peak in the positions of the ionization front and contact discontinuity, at about  $t \sim 4000$  yrs, corresponds to the first large eddy to be shed by the bowshock. The thickness of the shocked stellar wind region changes in response to pressure changes across the subsonic region, either due to the formation of instabilities or dynamics in the photoionized part of the shell.

Interestingly, the position of the contact discontinuity in Figure 23 is settling down (after 40,000 yrs) to a value close to  $\approx 1.5 r_0$ , which was predicted by van Buren & McCray (1988) from a simple model approximating the dynamics in the shocked wind by sonic flow in a hemispheric region between the stellar wind shock and the contact discontinuity. However, van Buren et al. (1990) argued that cooling via conduction in the shocked stellar wind would be so rapid that this layer would be very thin and its dynamics governed by momentum conservation. We do not include thermal conduction in the present models but suspect that it will not play as important a role as invoked by van Buren et al. (1990). The importance of conduction fronts for the cooling of stellar wind bubbles has been cast into doubt by the discovery of diffuse X-ray emission from high-mass star-forming regions, which suggests that the shocked stellar winds inside H II regions

do not cool efficiently (Townsend et al. 2005). It is probable that conduction is greatly reduced by the presence of magnetic fields. Our results show that instabilities at early times in the shocked wind layer do enhance cooling and affect its thickness. However, this is only a transient feature, and once the initial instabilities have been advected away from the bowshock head, the shocked stellar wind region is able to expand.

### 5.3. Champagne flow plus stellar motion

The density gradient plays a key role as to whether the dominant flow characteristic is champagne-flow-like or bowshock-like. In the steeper density gradient (Models G and H), a champagne flow sets up first, within which the stellar wind bubble develops, as for Model C. However, stellar motion ensures that the outer stellar wind shock rapidly overtakes the shock ahead of the ionization front. The redshifted velocity of the ionized gas ahead of the star is less than it would be for a bowshock in a neutral medium because of the photoevaporated flow set up by the density gradient, which is blueshifted. The density gradient in the neutral material ahead of the moving star increases the ram pressure acting on the stellar wind and the photoionized shell. Both the shocked stellar wind zone and the ionized shell become thinner ahead of the star as it travels up the density gradient, with the shocked stellar wind zone almost disappearing. This is more pronounced in Model H, where the faster-moving star reaches higher density regions than the slower star of Model G. Because the shocked stellar region ahead of the star becomes extremely thin, it is essentially the ram pressure of the free-flowing wind which balances that of the stellar motion through the ambient medium. At the sides of the structure, a champagne flow is still in evidence and the pressure of the photoionized gas confines the stellar wind (see Figure 12).

In the shallow density gradient (Model I), on the other hand, the swept-up shell formed by the stellar wind confines the ionization front before a champagne flow has chance to form. The outer stellar wind shock soon overtakes the shock ahead of the ionization front. The stellar wind bubble structure expands laterally downstream where the densities are lower and the swept-up shell becomes quite thick here. However, this never becomes a champagne flow (see, Figure 13). Ahead of the star the shocked stellar wind zone becomes thinner as the star advances up the density gradient, until it almost disappears and the ram pressure of the free-flowing wind balances that of the stellar motion through the ambient medium. The photoionized region ahead of the star is quite thick.

Although the stellar velocity in Model G is only  $5 \text{ km s}^{-1}$ , the projected velocity range shown in Figure 19 is  $\sim 15 \text{ km s}^{-1}$ , with the velocities becoming redshifted towards the tail where the champagne flow is important. The actual velocities at the head of the object are slightly redshifted compared to the background cloud, but the projected velocities at the head of the object are blueshifted, unlike in the simple bowshock case (see Figure 9). This shows that the pressure gradients within the shell due to the density distribution play an important role in advecting photoionized material in the shell at the head of the object round to the sides. Also, in projection we are seeing the near part of the champagne flow component, which has a strong influence on the projected velocities. The linewidths of this model also rise sharply towards the tail, reaching  $40 \text{ km s}^{-1}$ , suggestive of champagne flow. Model H also presents a projected velocity range of  $\sim 15 \text{ km s}^{-1}$  for a stellar speed of  $10 \text{ km s}^{-1}$ . The peak redshifted velocities in this model are just downstream of the

stellar position, and the peak linewidths are just ahead of it, which is more in keeping with a bowshock model. On the other hand, the velocities ahead of the star are blueshifted, as in Figure 19 for Model G, and this must be due to the influence of the density gradient. The velocities then become blueshifted again far down the tail.

The stellar speed in Model I is  $10 \text{ km s}^{-1}$  and the ionized gas velocities in the model ahead of the star are low and redshifted. However, even the shallow density gradient in this model ensures that the projected velocities ahead of the stellar position are blueshifted (see Figure 21) and become redshifted in the tail before turning blueshifted again. The full velocity range for this model is only about  $8 \text{ km s}^{-1}$ , principally due to the shallow density gradient. The linewidths are highest around the projected stellar position.

These combined models show that stellar motion in a density gradient has important differences to the standard bowshock model. In particular, the velocity range is larger than that for the case of stellar motion only (e.g., Model B) and the radial velocities change sign along the length of the object. These models are not hugely different from the champagne flow plus stellar wind cases, except that since there is effectively no shocked stellar wind zone ahead of the star (at least in the cases we have studied), then the peak emission occurs closer to star (see Figures 7 and 14).

The intention of Models G, H and I is to investigate what happens to the dynamics when density gradients, stellar winds and stellar motion are combined. In particular, we have not been overly concerned that the stars in our models start from low density regions. However, we could postulate a scenario in which stars, under the influence of the gravitational field of a molecular cloud, move in and out of local density peaks, and that our models represent a particular stage in this picture. Another possibility is that an external shock triggers star formation in the outer parts of a cloud and that, once formed, the massive star continues to coast in towards the cloud center, or is attracted to the center by the gravity of the main cloud core. In any case, the low density material is quickly advected off grid and replaced by either photoevaporated flow material (Models G and H) or material advected round the photoionized shell from the region of the head by the pressure gradient (Model I). In either case, the details of the initial environment are quickly lost by the model as it advances up the density gradient.

Franco et al. (2005) have recently studied the evolution of H II regions in dense, structured molecular clouds where the star starts from a dense core and travels down the density gradient. They do not include the effect of stellar winds or discuss the dynamics of the ionized gas. The velocities of the stars vary between  $2$  and  $12 \text{ km s}^{-1}$  (i.e., subsonic and supersonic with respect to the ionized gas). It is found that for slow moving stars a champagne flow dominates, while for the faster moving stars a “bow” shape is formed when the star overtakes the ionized gas in expansion, since the gas can only expand at the sound speed and the star is moving supersonically. In the high density regions the star has left behind the gas recombiners. This is an interesting scenario but unfortunately the authors do not include any analysis of the kinematics. It is probable that the inclusion of a stellar wind will modify the faster case, since the stellar velocity is not supersonic with respect to the stellar wind and the direction of motion is towards decreasing densities, so the ram pressure of the ambient medium is decreasing (or constant). In our models, the ram pressure increases as the star moves up the density gradient

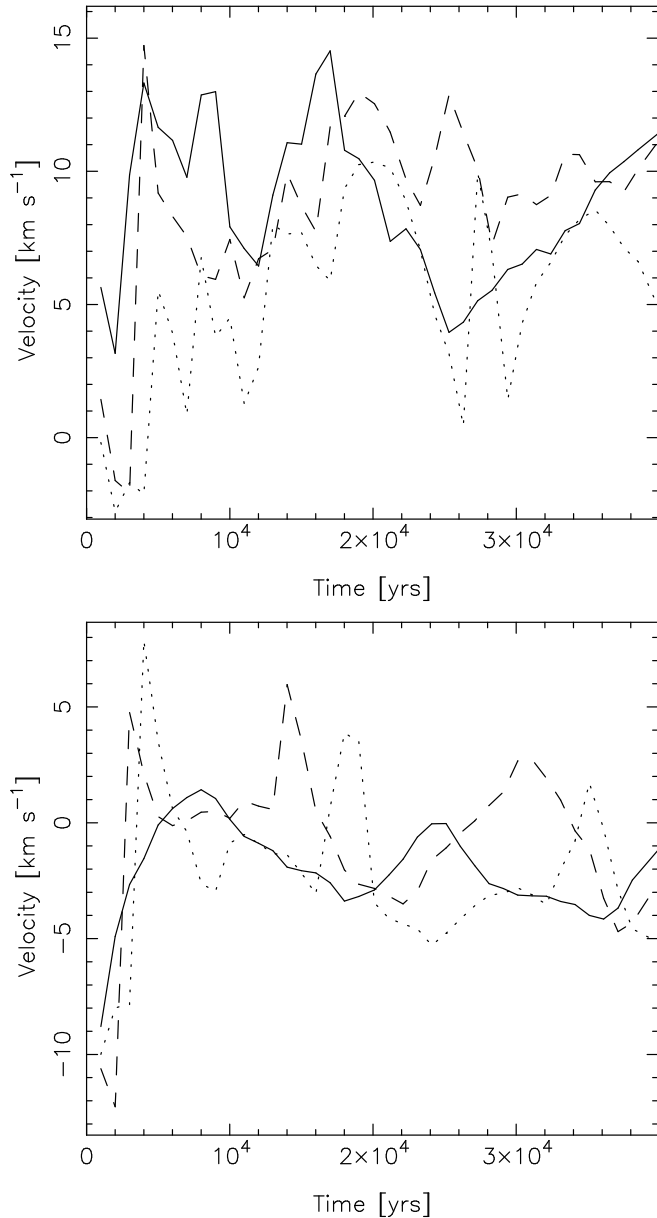


FIG. 24.— Time evolution of projected velocities at half peak flux (solid line), quarter peak flux (dashed line) and one eighth peak flux (dotted line) for inclination angle  $i = 45^\circ$ : Top panel—Model B (bowshock); Bottom panel—Model C (champagne flow plus stellar wind).

and so it is quite possible that the star overtakes the swept-up wind shell with its trapped ionization front if the evolution is followed for long enough.

#### 5.4. Effect of Eddies

In Figure 24 we examine the evolution of the line-of-sight velocity at half, quarter and one eighth of the peak flux along the symmetry axis of the numerical model for an inclination angle of  $i = 45^\circ$ . The large peaks in these curves correspond to eddies being shed from the head of the cometary H II region and travelling downstream, hence there is a phase lag between peaks on each line. In the champagne flow plus stellar wind case an “average” profile can be discerned for each curve. However, in the bowshock case the curves are far too noisy. It is not possible to draw any conclusions from these

plots to aid as a diagnostic tool for discriminating between bowshock and champagne flow plus stellar wind models. We note that in the bowshock case there appears to be a slight trend for the velocities further down the slit to rise with time, while in the champagne flow plus stellar wind case there is a trend for all velocities to become slowly more blueshifted with time.

The spectra obtained by, e.g., Lumsden & Hoare (1996, 1999) are not as noisy as our theoretical spectra. This could partially be due to the resolution of the observations, but it also suggests that the eddies we see forming in our simulations are dissipated more quickly in reality. In order to investigate this possibility numerically, we would have to incorporate a turbulence model, such as that outlined by Falle (1994), in our numerical scheme. This is beyond the scope of the present paper.

### 5.5. Comparison with observations

#### 5.5.1. G29.96–0.02

G29.92–0.02 is, perhaps, the most well studied of all cometary ultracompact H II regions. It was first observed by Wood & Churchwell (1989) at radio wavelengths. The morphology of this region is that of a bright arc of emission at the head trailing off into a low-surface brightness tail. The background cloud systemic velocity is best determined from molecular line observations, which trace the bulk of the gas. Both single dish (Churchwell et al. 1992; Kim & Koo 2003) and interferometric (Pratap et al. 1999; Olmi et al. 2003) observations of optically thin CO and CS lines give velocities of 97–98 km s<sup>-1</sup>.

The infrared observations of Lumsden & Hoare (1996, 1999), Martín-Hernández et al. (2003) and Zhu et al. (2005) provide the most detailed kinematic results of G29.96–0.02 with which to compare our numerical simulations. Lumsden & Hoare (1996) and Martín-Hernández et al. (2003) obtained long slit spectra of the Bry hydrogen recombination line, while Zhu et al. (2005) obtained mid-infrared observations of the [Ne II] 12.8  $\mu\text{m}$  fine-structure line. These fine-structure line studies are particularly promising because the FWHM line width due to thermal broadening of Ne<sup>+</sup> at 10<sup>4</sup> K is only  $\sim 4.8$  km s<sup>-1</sup>, whereas that of H<sup>+</sup> is  $\sim 21$  km s<sup>-1</sup>, hence the kinematics of the ionized gas can be separated from the thermal and turbulent broadening contributions if the velocity resolution of the observations is good enough (as long as the Ne<sup>+</sup> ion is present in the whole volume).

These detailed observational studies find a radial velocity range of  $\sim -15$  to  $\sim +10$  km s<sup>-1</sup> for the ionized gas with respect to the molecular cloud (assuming a background cloud velocity of 98 km s<sup>-1</sup>), with the highest blue-shifted velocities ahead of the emission peak of the object, red-shifted velocities behind the emission peak and blue-shifted velocities again in the tail. The line widths of the Bry data are highest at the head, as are the [Ne II] line widths. In the past, this object has been modeled as a bowshock H II region, with an inferred stellar motion of 20 km s<sup>-1</sup> in order to give the velocity range (e.g., Afllerbach et al. 1994; Lumsden & Hoare 1996; Martín-Hernández et al. 2003; Zhu et al. 2005). However, for a slit placed along the symmetry axis of the cometary H II region, simple bowshock models give either wholly red-shifted or wholly blueshifted velocities with respect to the background cloud, depending on the angle of inclination to the line of sight. For this reason, several authors (Lumsden & Hoare 1996, 1999; Martín-Hernández et al. 2003; Zhu et

al. 2005) have argued that a simple bowshock model cannot reproduce the observed velocity behavior. Although a stellar velocity of  $20 \text{ km s}^{-1}$  can give the observed velocity range, it cannot reproduce the velocity offset with respect to the molecular cloud, which requires a lower stellar velocity. On the other hand, simple champagne flow models would not give a limb-brightened morphology, nor reproduce the velocity and linewidth behavior. Lumsden & Hoare (1996) suggested that stellar winds and density gradients might be important for the kinematics of this object, while Zhu et al. (2005) argued that pressure gradients within the parabolic shell are needed to increase the velocity range.

Our numerical models comprising a star with a stellar wind in a density gradient (e.g., Models C, G, H and I) can all reproduce the blueshifted to redshifted to blueshifted velocity behavior exhibited by G29.96–0.02, together with a strong, arc-like emission at the head, assuming an inclination angle of  $45^\circ$  to the line of sight. However, the maximum velocity range our models achieve is only  $\sim 15 \text{ km s}^{-1}$  before the flux drops below 1% of the peak value, as against the  $\sim 20$  to  $25 \text{ km s}^{-1}$  seen in the observations. The velocity range increases as the density gradient becomes steeper, so it is conceivable that a steeper gradient than the ones we have investigated would give the observed velocity range. The spatial variation of the flux of  $\text{Br}\gamma$  along the symmetry axis in the high resolution observations of Martín-Hernández et al. (2003) bears a striking resemblance to that of our Model I, as does the variation of the velocity centroid of the same line along the slit (ignoring the blue-shifted shoulder seen in the observations, which appears to be unconnected with the H II region and is probably due to motions associated with the nearby hot core source). Even the “knee” in the observed  $\text{Br}\gamma$  flux, also present in the  $[\text{Ne II}]$  observations of Zhu et al. (2005), is seen in the model (where it is due to the line of sight cutting through thick, dense regions of ionized shell on both sides of the star), although this is serendipitous. Models C, G and H, however, have a larger velocity range than Model I. The linewidths in Models H and I are highest at the head of the object for this slit, although not ahead of the peak emission, as seen in the observations by Lumsden & Hoare (1996, 1999) and Martín-Hernández et al. (2003). The large linewidths seen in Model I are most likely due to instabilities in the photoionized shell and are thus transient. The linewidths in Model H, on the other hand, appear to be the result of the general flow pattern.

The  $\text{H}_2$  observed in this object comes from the region outside of the ionization front. However, it is not likely to come from the quiescent background cloud, rather it arises in the region between the shock ahead of the ionization front in the neutral medium and the ionization front, probably due to fluorescence, and thus will have a red-shifted velocity with respect to the cloud and the ionized gas. This is suggested by the observations reported by Martín-Hernández et al. (2003), where the  $\text{H}_2$  is redshifted by  $\sim 2 \text{ km s}^{-1}$  with respect to the background cloud velocity as determined from molecular line observations. Our models show that a shock front advances slowly into the neutral medium with velocities of order a few  $\text{km s}^{-1}$ , which is consistent with this velocity redshift.

The parameters of the numerical models have not been tailored to fit G29.96–0.02, but the qualitative agreement is encouraging. We have shown that models including a strong stellar wind and a density gradient are able to reproduce the morphology, velocity behavior, and to some extent the linewidth behavior of this object. Stellar motion appears to modify the line-width behavior of an essentially champagne-type

flow and so we suggest that G29.96–0.02 could be the H II region formed by a star with a strong stellar wind in a density gradient, possibly with the star moving up the gradient.

### 5.5.2. Hydrogen radio recombination line studies

A detailed examination of  $\text{H}92\alpha$  radio recombination line observations of three cometary H II regions was presented by Garay et al. (1994). They found velocity ranges of up to  $12 \text{ km s}^{-1}$  between the head and tail regions of these objects. Two of these objects were interpreted as champagne flows, mainly because the velocities at the head were approximately equal to the background cloud velocities as measured from observations of  $\text{NH}_3$ . The third object was interpreted as a bowshock flow since the velocities were all redshifted with respect to the background cloud. However, even in a simple photoevaporated champagne flow model such as that presented in Model A, we would expect to find a velocity shift between the ionized gas at peak emission and the background cloud (unless the object is in the plane of the sky), since the gas leaves the ionization front with a velocity about half the sound speed and then accelerates (see, e.g., Figure 8). Also, in the champagne flow objects, the linewidth variations between head and tail are not entirely consistent with the champagne flow interpretation: in one object the linewidths decrease towards the tail and in the other they are roughly constant.

Garay et al. (1994) discuss the possibility that the stellar wind modifies the flow, but their analytic treatment requires the star to be at the center of a radially decreasing density distribution. In our models we are able to place the star and its stellar wind at arbitrary points in density distributions with steep and shallow gradients. We find that the combination of a stellar wind and a density gradient changes the linewidth behavior, since the ionized flow is forced to flow around the outside of the stellar wind bubble (e.g., Models C, E and F).

Cyganowski et al. (2003) have recently reported hydrogen recombination line radio observations of dual cometary H II regions in DR 21. The radial velocities of the ionized gas suggest a bowshock interpretation since they are higher at the head. However, for one of the H II regions, it is reported elsewhere (Roelfsema et al. 1989) that velocities down the tail become increasingly redshifted with respect to the background cloud, while velocities at the head are blueshifted. Furthermore, the linewidths for both objects suggest that there is an increase towards the tail, which is not expected for a bowshock model. Models incorporating stellar winds and density gradients, such as our Models C, F and G, can demonstrate this spatial variation in velocity and linewidth. The “hybrid” picture developed by Cyganowski et al. (2003) to explain the motions they see in DR 21 has some similarities with our models.

From observations of the neutral, atomic and molecular gas associated with the cometary H II region G111.67+0.37, Lebrón et al. (2001) find that both the neutral and ionized gas exhibit velocity gradients from the head to the tail of the cometary region, but that the neutral gas has a lower velocity range than the ionized gas and is detected principally towards the tail where the PDR is thickest. Our numerical models also demonstrate this behavior. Although we do not show results for the neutral gas here, it will be the subject of a future paper.

## 6. CONCLUSIONS

We have performed numerical simulations of cometary H II regions forming in media with density gradients and where the ionizing star may additionally have either or both a strong

stellar wind and a supersonic motion with respect to the neutral gas. Analysis of our results and a comparison with observations from the literature show that:

1. Photoevaporated champagne flow models with stellar winds can have limb-brightened morphologies, which simple champagne flows cannot. This is because the stellar wind bubble acts as an obstacle to the photoevaporated flow, which must divert around it.
2. Depending on the steepness of the density gradient, the morphologies of the champagne flow plus stellar wind models can appear more limb-brightened (steep gradient) or more shell-like (shallow density gradient).
3. In the absence of thermal conduction, numerical bowshock simulations (in uniform media) are not well described by momentum-conserving, ram pressure balance analytical models. This is because the shocked stellar wind does not cool efficiently and its thermal pressure must also be taken into account.
4. In both champagne type models and bowshock models a shock runs ahead of the ionization front in the neutral material. Typical velocities in the neutral gas behind these shocks are a few  $\text{km s}^{-1}$ . These velocities could influence  $\text{H}_2$  and carbon recombination line measurements of the systemic cloud velocity, since this emission is most likely to come from the photon dominated region, which is a thin region just outside the ionization front and thus wholly contained in the zone behind the shock in the neutral gas.
5. Models in which a star with a strong stellar wind advances supersonically up a density gradient are champagne-flow dominated if the gradient is steep enough and stellar wind shell dominated if the density gradient is shallow. These models produce limb-brightened H II regions. In these models, the shocked stellar wind region is extremely thin due to the increasing ram pressure as the star advances up the density gradient, and the fact that the shocked wind material is quickly advected away from the region of the head due to the density gradient.
6. Models of stars with stellar winds moving in density gradients result in the peak emission being closer to the star than for similar models without stellar motion because the shocked stellar wind zone is extremely thin and so the photoionized shell is closer to the star.
7. The radial velocity range of  $\sim 20 \text{ km s}^{-1}$  seen in observations, coupled with a limb-brightened morphology,

can be reproduced either by a fast-moving  $\sim 20 \text{ km s}^{-1}$  star or by a star with a stellar wind in a steep density gradient. The key observational discriminant is the radial velocity pattern along the object with respect to the ambient material. For an inclination angle of  $i = 45^\circ$  to the line of sight, for example, the velocities of the bowshock model will all be redshifted with respect to the ambient cloud, whereas the champagne flow plus stellar wind model gives blueshifted velocities at the head, redshifted velocities around the stellar position, and blueshifted velocities again in the tail. Similar velocity behavior is seen in the models that also include stellar motion, showing that for the modest stellar velocities considered ( $5$  and  $10 \text{ km s}^{-1}$ ), the density gradient is more important than the star's speed for determining the velocities in the photoionized shell.

8. The linewidths in simple champagne flow models are highest in the tail of the cometary H II region, while those of bowshock models are highest ahead of the star. In our models combining density gradients, stellar winds and stellar motion we find that the champagne flow dominated flows (slow-moving star in steep density gradient) have larger velocity widths towards the tail, while for faster moving stars in shallow density gradients the largest line widths occur further up the cometary structure at the stellar position. Such intermediate linewidth information is also reported in observations.

Our results show that the most likely explanation for the observed morphologies and kinematics of cometary compact H II regions is the outcome of ionizing stars with strong stellar winds in density gradients, possibly with the star moving up the gradient. It is important to obtain a reliable determination of the systemic cloud velocity in order to be able to discriminate between possible models.

We thank Will Henney for valuable comments and a critical reading of the manuscript. SJA would like to acknowledge support from DGAPA-PAPIIT grants IN115202 and IN112006-3, and for financial support from DGAPA-UNAM during a year's sabbatical visit to the University of Leeds. Some of the numerical simulations in this paper were performed on a linux cluster at CRyA funded by CONACyT grant 36571-E to Enrique Vázquez-Semadeni. We thank the anonymous referee for constructive comments which improved the presentation of this paper. This work has made extensive use of NASA's Astrophysics Abstract Data Service and the astro-ph archive.

#### REFERENCES

- Afflerbach, A., Churchwell, E., Hofner, P., & Kurtz, S. 1994, *ApJ*, 437, 697  
 Arquilla, R., & Goldsmith, P. F. 1985, *ApJ*, 297, 436  
 Arthur, S. J., & Falle, S. A. E. G. 1993, *MNRAS*, 261, 681  
 Arthur, S. J., Kurtz, S. E., Franco, J., & Albarrán, M. Y. 2004, *ApJ*, 608, 282  
 Bedijn, P. J., & Tenorio-Tagle, G. 1981, *A&A*, 98, 85  
 Bodenheimer, P., Tenorio-Tagle, G., & Yorke, H. W. 1979, *ApJ*, 233, 85  
 Chevalier, R. A., & Clegg, A. W. 1985, *Nature*, 317, 44  
 Churchwell, E., Walmsley, C. M., & Wood, D. O. S. 1992, *A&A*, 253, 541  
 Comerón, F. 1997, *A&A*, 326, 1195  
 Comerón, F., & Kaper, L. 1998, *A&A*, 338, 273  
 Cyganowski, C. J., Reid, M. J., Fish, V. L., & Ho, P. T. P. 2003, *ApJ*, 596, 344  
 De Pree, C. G., Wilner, D. J., Deblasio, J., Mercer, A. J., & Davis, L. E. 2005, *ApJ*, 624, L101  
 Dyson, J. E. 1977, *A&A*, 59, 161  
 Dyson, J. E., & Williams, D. A. 1997, *The physics of the interstellar medium*. Edition: 2nd ed. Publisher: Bristol: Institute of Physics Publishing, 1997. Edited by J. E. Dyson and D. A. Williams. Series: The graduate series in astronomy. ISBN: 0750303069,  
 Falle, S. A. E. G. 1975, *A&A*, 43, 323  
 Falle, S. A. E. G. 1994, *MNRAS*, 269, 607  
 Fich, M. 1993, *ApJS*, 86, 475  
 Franco, J., García-Barreto, J. A., & de la Fuente, E. 2000, *ApJ*, 544, 277  
 Franco, J., García-Segura, G., & Kurtz, S. E. 2005, *astro-ph/0508467*  
 Franco, J., Kurtz, S., Hofner, P., Testi, L., García-Segura, G., & Martos, M. 2000, *ApJ*, 542, L143  
 Franco, J., Tenorio-Tagle, G., & Bodenheimer, P. 1990, *ApJ*, 349, 126



- Franco, J., Tenorio-Tagle, G., & Bodenheimer, P. 1989, *Revista Mexicana de Astronomia y Astrofisica*, vol. 18, 18, 65
- Freyer, T., Hensler, G., & Yorke, H. W. 2003, *ApJ*, 594, 888
- Garay, G., Lizano, S., & Gomez, Y. 1994, *ApJ*, 429, 268
- García-Arredondo, F., Henney, W. J., & Arthur, S. J. 2001, *ApJ*, 561, 830
- García-Arredondo, F., Arthur, S. J., & Henney, W. J. 2002, *Revista Mexicana de Astronomia y Astrofisica*, 38, 51
- García-Segura, G., & Mac Low, M.-M. 1995, *ApJ*, 455, 160
- García-Segura, G., & Franco, J. 1996, *ApJ*, 469, 171
- García-Segura, G., Mac Low, M.-M., & Langer, N. 1996, *A&A*, 305, 229
- Gaume, R. A., Fey, A. L., & Claussen, M. J. 1994, *ApJ*, 432, 648
- Godunov, S. K. 1959, *Mat. Sbornik*, 47, 271
- Hatchell, J., & van der Tak, F. F. S. 2003, *A&A*, 409, 589
- Henney, W. J., Arthur, S. J., & García-Díaz, M. T. 2005, *ApJ*, 627, 813
- Hoare, M. G., Lumsden, S. L., Busfield, A. L., & Buckley, P. 2003, *Revista Mexicana de Astronomia y Astrofisica Conference Series*, 15, 172
- Hofner, P., Wyrowski, F., Walmsley, C. M., & Churchwell, E. 2000, *ApJ*, 536, 393
- Icke, V., Gatley, I., & Israel, F. P. 1980, *ApJ*, 236, 808
- Israel, F. P. 1978, *A&A*, 70, 769
- Jaffe, D. T., Zhu, Q., Lacy, J. H., & Richter, M. 2003, *ApJ*, 596, 1053
- Kahn, F. D. 1954, *Bull. Astron. Inst. Netherlands*, 12, 187
- Kim, K.-T., & Koo, B.-C. 2003, *ApJ*, 596, 362
- Kunasz, P., & Auer, L. H. 1988, *Journal of Quantitative Spectroscopy and Radiative Transfer*, 39, 67
- Kurtz, S., Churchwell, E., & Wood, D. O. S. 1994, *ApJS*, 91, 659
- Lebrón, M. E., Rodríguez, L. F., & Lizano, S. 2001, *ApJ*, 560, 806
- Lumsden, S. L., & Hoare, M. G. 1996, *ApJ*, 464, 272
- Lumsden, S. L., & Hoare, M. G. 1999, *MNRAS*, 305, 701
- Mac Low, M.-M., van Buren, D., Wood, D. O. S., & Churchwell, E. 1991, *ApJ*, 369, 395
- Martín-Hernández, N. L., Bik, A., Kaper, L., Tielens, A. G. G. M., & Hanson, M. M. 2003, *A&A*, 405, 175
- Martins, F., Schaerer, D., & Hillier, D. J. 2005, *A&A*, 436, 1049
- Mihalas, D., Auer, L. H., & Mihalas, B. R. 1978, *ApJ*, 220, 1001
- Olmí, L., Cesaroni, R., Hofner, P., Kurtz, S., Churchwell, E., & Walmsley, C. M. 2003, *A&A*, 407, 225
- Panagia, N. 1973, *AJ*, 78, 929
- Pratap, P., Megeath, S. T., & Bergin, E. A. 1999, *ApJ*, 517, 799
- Quirk, J. J. 1994, *Internat. J. Numer. Methods Fluids*, 18, 555
- Raga, A. C., Noriega-Crespo, A., Cantó, J., Steffen, W., van Buren, D., Mellema, G., & Lundqvist, P. 1997, *Revista Mexicana de Astronomia y Astrofisica*, 33, 73
- Raga, A. C., Mellema, G., Arthur, S. J., Binette, L., Ferruit, P., & Steffen, W. 1999, *Revista Mexicana de Astronomia y Astrofisica*, 35, 123
- Roelfsema, P. R., Goss, W. M., & Geballe, T. R. 1989, *A&A*, 222, 247
- Roshi, D. A., Goss, W. M., Anantharamaiah, K. R., & Jeyakumar, S. 2005, *ApJ*, 626, 253
- Rozyczka, M. 1985, *A&A*, 143, 59
- Ryu, D., & Vishniac, E. T. 1987, *ApJ*, 313, 820
- Ryu, D., & Vishniac, E. T. 1988, *ApJ*, 331, 350
- Sanders, R., Morano, E., & Druguet, M.-C. 1998, *J. Comp. Phys.*, 145, 511
- Spitzer, L. 1978, *Physical Processes in the Interstellar Medium* (New York: John Wiley)
- Strömgren, B. 1939, *ApJ*, 89, 526
- Tenorio-Tagle, G. 1979, *A&A*, 71, 59
- Teixeira, P. S., Lada, C. J., & Alves, J. F. 2005, *ApJ*, 629, 276
- Townsley, L. K., Broos, P. S., Feigelson, E. D., & Garmire, G. P. 2005, *IAU Symposium*, 227, 297
- van Buren, D., Mac Low, M.-M., Wood, D. O. S., & Churchwell, E. 1990, *ApJ*, 353, 570
- van Buren, D., & Mac Low, M.-M. 1992, *ApJ*, 394, 534
- van Buren, D., & McCray, R. 1988, *ApJ*, 329, L93
- van Leer, B. 1982, in *Lecture Notes in Physics*, Vol. 170, ed. E. Krause (Springer-Verlag), 507
- Vishniac, E. T. 1983, *ApJ*, 274, 152
- Vishniac, E. T. 1994, *ApJ*, 428, 186
- Vishniac, E. T., & Ryu, D. 1989, *ApJ*, 337, 917
- Walsh, A. J., Burton, M. G., Hyland, A. R., & Robinson, G. 1998, *MNRAS*, 301, 640
- Weaver, R., McCray, R., Castor, J., Shapiro, P., & Moore, R. 1977, *ApJ*, 218, 377
- Wilkin, F. P. 1996, *ApJ*, 459, L31
- Williams, R. J. R. 1999, *MNRAS*, 310, 789
- Wood, D. O. S., & Churchwell, E. 1989, *ApJS*, 69, 831
- Wood, D. O. S., & Churchwell, E. 1991, *ApJ*, 372, 199
- Yorke, H. W., Tenorio-Tagle, G., & Bodenheimer, P. 1983, *A&A*, 127, 313
- Zhu, Q.-F., Lacy, J. H., Jaffe, D. T., Richter, M. J., & Greathouse, T. K. 2005, *ApJ*, 631, 381